ABSTRACT

Title of thesis: QUASI-ONE-DIMENSIONAL MODELING OF AN ADIABATIC-COMPRESSION PREHEATED LUDWIEG TUBE

Joseph Chung, Master of Science, 2015

Thesis directed by: Professor Stuart Laurence
Department of Aerospace Engineering

A novel hypersonic facility is proposed that will reproduce the high pressures and temperatures necessary for the accurate simulation of hypersonic flight conditions. It will provide sufficient test times for investigating unsteady, transient flow effects while maintaining high flow quality due to the absence of vitiation contaminants and shocks in the generating flow. An electrically preheated Ludwieg tube provides the initial means of heating while the piston-compression is used to further increase the pressure and temperature. Preliminary constraints on the design space for optimal operation are presented through the method of characteristics (MOC). Further characterization is performed with quasi-one-dimensional Euler computations. The MOC approach shows the optimal operating condition constrains the compression ratio and Ludwieg tube to nozzle exit diameter ratio, assuming proper simulation of flight conditions. The unsteady Euler computations predict the presence of pressure oscillations generated during the piston-compression process. Methods are investigated to mitigate these oscillations.

QUASI-ONE-DIMENSIONAL MODELING OF AN ADIABATIC-COMPRESSION PREHEATED LUDWIEG TUBE

by

Joseph Chung

Thesis submitted to the Faculty of the Graduate School of the
University of Maryland, College Park in partial fulfillment
of the requirements for the degree of
Master of Science
2015

Advisory Committee:
Professor Stuart J. Laurence, Chair/Adviser
Professor Kenneth H. Yu
Professor Ryan Houim

Acknowledgments

I would like to thank my adviser, Dr. Stuart Laurence, for providing me the opportunity to work with him and this project. His patience, support, and guidance is immensely appreciated.

Dr. Ryan Houim has provided immense support in the numerical methodology for this work, for which I am extremely grateful. His guidance and patience through the computational development was truly unexpected and is something I am indebted to.

I would like to thank Dr. Yu for guiding my initial steps through this experience and agreeing to be on my committee. His guidance through my educational career has been invaluable.

Finally, I appreciate the support of my office-mates and also those who do not share the office with me.

Table of Contents

List of Figures

Chapter 1: Introduction

The accurate replication of hypersonic flight conditions (Mach number, temperature, pressure, and flow composition) by a single ground-test facility is often limited by cost and complexity. For simulations involving scramjet combustors, many researchers turn to either direct-connect facilities which simulate the conditions entering the combustor, or free-jet facilities which simulate the free-stream conditions of the scramjet inlet, allowing for the modeling of the entire scramjet flowpath (sub or full-scale). These facilities simulate hypersonic conditions by expanding a high-enthalpy, high-pressure flow through a converging-diverging nozzle. Although the requirement of total-enthalpy reproduction is often relaxed for purely aerodynamic or aerothermodynamic testing at lower hypersonic Mach numbers (5-7), matching the correct total-enthalpy is especially critical for an accurate simulation of flows involving combustion. Direct-connect facilities typically match the flight enthalpy of lower Mach numbers (4 - 7) while free-jet facilities include and extend available testing conditions well beyond this range.

The high-temperatures necessary for accurately simulating combustion in the supersonic flows seen in scramjet combustors present difficult challenges in the design, development, and operation of these facilities. Many compromise test time,

flow quality, and/or cost to achieve their desired test conditions. A novel, free-jet facility (with potential direct-connect capability) is proposed to be built at the University of Maryland that addresses these compromises by matching temperature, pressure, and chemical composition while providing high flow quality with sufficient test times, at low operational cost. This work presents the operational concept of the proposed facility, the calculation of its available conditions, and the unsteady quasi-one-dimensional numerical modeling used to determine the potential quality of the test flow.

1.1 High Temperature Hypersonic Facilities

Scramjet ground-testing facilities can be loosely categorized into two areas: direct-connect and free-jet. Direct-connect facilities simulate the entrance conditions of the scramjet combustor, allowing for relaxed constraints on total-pressure reproduction. They are used to assess and characterize the mixing, ignition, and flameholding performance of a combustor. While traditionally providing long test times, they are unable to model the inlet influence on the combustor which would require a fully integrated scramjet flowpath. Free-jet facilities simulate the free-stream conditions of the scramjet flight path, allowing for the full (sometimes partial) experimental integration of its internal flowpath components. This added capability comes at the cost of requiring higher pressures and larger scale facilities; in addition, due to energy and size limitations, sacrifices are often made in available test times.

1.1.1 Direct-Connect Facilities

An example of a direct-connect facility with clean flow quality is the electrically heated facility of University of Virginia (UVA) [1]. This facility is vertically mounted, with the high pressure reservoir at the bottom, a converging-diverging nozzle, then an isolator which leads into the combustor; the exhaust gas is ejected into atmospheric conditions rather than into an evacuated dump tank. The experiments performed in this facility have traditionally focused on dual-mode combustors, which are designed for both subsonic and supersonic combustion. It provides clean flow quality with nearly continuous testing capability, but material limitations restrict reservoir temperatures to 1200 K (equivalent to a freestream Mach number of 5), making it undesirable for purely hypersonic scramjet testing.

One example of a high-enthalpy vitiated direct-connect facility is the vitiated-air generator blown tunnel (VAG) of Kakuda Research Center, National Aerospace Laboratory in Japan [2]. It can attain stagnation temperatures up to 2700 K with 4 seconds of steady test time. The combustion of hydrogen provides the heating source with additional oxygen supplied to the test flow to match atmospheric mole fractions. Similar facilities exist in the United States, one being the direct-connect supersonic combustion test facility at the NASA Langley Research Center Scramjet Test Complex [7]. This facility has a 2100 K stagnation temperature capability, again with the added complexity of oxygen replenishment and fuel pressure regulation.

The supersonic combustion facility at the University of Michigan [8] is a hybrid

direct-connect facility utilizing both an electric heater and hydrogen vitiation. The stagnation temperatures here can reach 1800 K for a test time of 2 seconds, with longer test times available at lower temperatures (for example, 10 seconds at 1400 K).

However, the drawbacks of using a vitiated test gas were demonstrated by an experimental comparison [2] performed between the VAG vitiated test gas and a non-vitiated test gas with similar stagnation temperatures and pressures (1600 K and 47 MPa). The vitiated test gas induced a higher likelihood of autoignition within the scramjet combustor when compared to the non-vitiated condition, which in the latter case was only possible in the boundary layer. They attribute this phenomenon to radicals introduced into the test flow, generated by the vitiation process. However, the vitiated gas also changed the location of the flame, moving it downstream to the divergent section of their combustor. This is attributed to the increased water content from the heating process. For the same equivalence ratios and combustor entrance conditions (except for chemical composition), they found reduced thrust performance with the vitiated gas. Scram to ram mode transition also occurred at nearly twice the fuel flow rate for the vitiated condition. The critical result from this study is that combustion characteristics and transition within the test combustor can change drastically when combustion is used to heat the generating flow.

Another experimental study [3] was carried out at the UVA electrically heated facility to investigate the effects of vitiation gas on scramjet combustion. The results agree with [2] in nearly all aspects. In this experiment, additional contaminants (H_2O, CO_2) were added to a heated clean flow. With the introduction of water va-

por, the experiments also saw reduced thrust, the flame move downstream, and scram to ram mode transition occurring at higher equivalence ratios. These experiments also show that increasing the water mole fraction beyond 3% has diminishing effects on changing the combustor performance, suggesting hybrid-heating schemes offer little advantage compared to fully vitiated facilities.

1.1.2 Free-Jet Facilities

Various types of high enthalpy free-jet facilities exist, many employing different methods to heat the test flow from those seen in direct-connect facilities. The arc-heated facility of Notre-Dame [4] has a 4000 K stagnation temperature capability, with stagnation pressures up to 9 bar, and test times on the order of a second. Scramjet combustor experiments in this facility simulate only a partial inlet to account for the relatively low stagnation pressures. Although the high stagnation temperature allows for a wide range of operating conditions, experiments from this facility must also deal with contaminants from the arc-heating. This introduction of non-atmospheric chemical species can produce results uncharacteristic of flight conditions, as seen in the vitiated vs. non-vitiated comparison [2] and also numerical simulations for the NASA Langley arc-heated facility [9].

The hypervelocity expansion tube at the University of Illinois [ref] is a free-jet facility with no external flow contamination and extremely high stagnation temperatures of up to 8000 K. However, the small scale (9 m) of this facility leads to short test times, typically on the order of a few hundred micro-seconds. The longer expan-

sion tube at Stanford [6] (12 m) can increase this test time closer to a millisecond with similarly high stagnation temperatures and pressures. These expansion tunnels exploit the unsteady shock-expansion interaction to achieve these high stagnation conditions. The piston driven T5 reflected shock tunnel at Caltech [5] similarly exploits unsteady shock heating and compression of the test gas, utilizing a short-duration piston-compression process to pressurize the driver gas. At 45 meters in length, this facility is significantly longer than the previous two mentioned, allowing for up to 2 ms in test times. Their achievable stagnation temperature is 10,000 K at 100 MPa in stagnation pressure.

Although expansion and shock tunnels can provide atmospherically matched flow composition, the flow quality suffers from diaphragm contamination and noise resulting from a shock in the generating flow. Their extremely short test times can also limit investigations of unsteady flow.

1.2 Ludwieg Tubes

A Ludwieg tube is a simplified alternative to traditional blow-down wind tunnels that was introduced to reduce the costs associated with generating supersonic and hypersonic flows. Traditionally, facilities utilizing Ludwieg tubes have been used for strictly aerodynamic testing due to material heating limitations. Many hypersonic and supersonic Ludwieg tubes are in operation today [10] utilizing various methods to heat and pressurize the test fluid. An illustration oh the Ludwieg tube operation is presented in figure 1.1. The Ludwieg tube is initially pressurized with

a chosen test gas (which can be heated) while the test section, nozzle, and dump tank are evacuated. Once the chosen pressure is reached, the diaphragm bursts (or valve opens) discharging the gas in the Ludwieg tube. This gas moves through a converging-diverging nozzle and is supersonically expanded to the desired test condition. A subsequent expansion wave moves towards the opposite end of the tube (left in figure 1.1), which then reflects off the end wall and eventually arrives back at the nozzle. Until the time of the expansion returning, the conditions within the Ludwieg tube are nearly steady. The test time here is limited by the length of the tube and the speed of sound of the test gas.

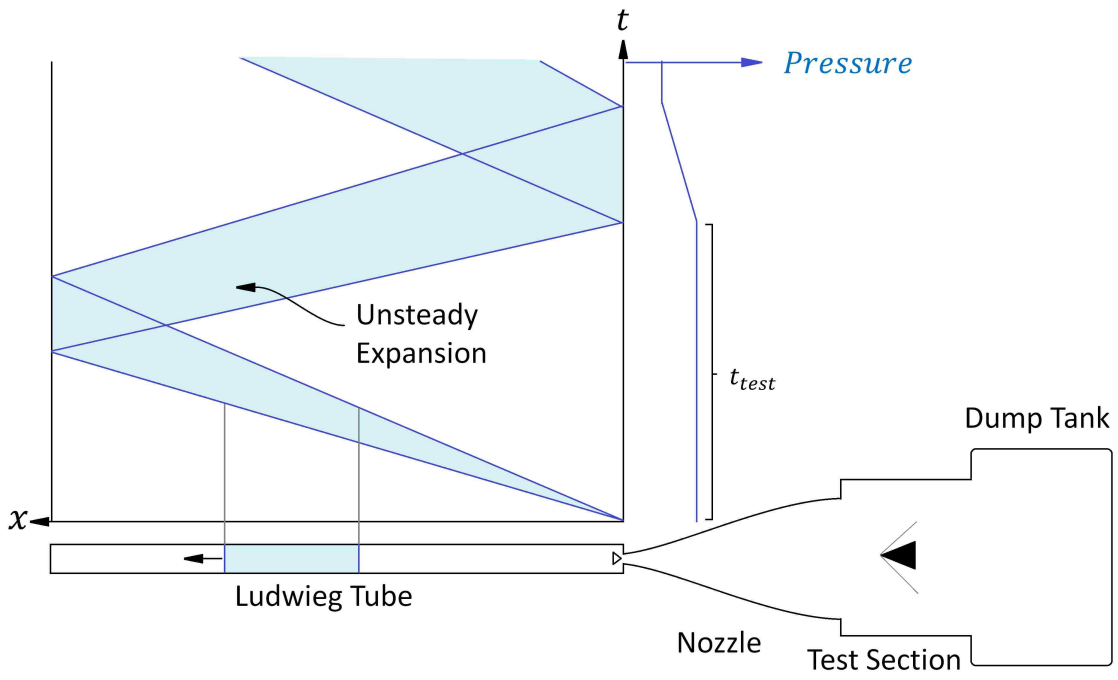

Figure 1.1: Illustration of a traditional Ludwieg tube operation.

The Ludwieg tube is essentially a specialized blow-down wind tunnel that exploits a small region of steady conditions during the unsteady expansion process.

These facilities do not require any pressure or temperature regulation devices during the run time which greatly simplifies operation. The flow generated by the tube is extremely clean when compared to expansion or shock tunnels. Although the test times are generally limited to the order of tens of milliseconds, this is still significantly greater than what is available in shock and expansion tunnels (at the cost of lower stagnation temperature and pressures).

1.3 Proposed Facility

A challenge exists in developing a cost-effective hypersonic facility for accurate scramjet simulations. This is especially important for university level research, where the development and operational costs associated with larger facilities can be prohibitive. Vitiation heated test-flow can lead to undesirable effects on the test results whereas a solely electrically heated facility faces material limitations, preventing full simulation of hypersonic conditions. Shock and expansion tunnels can generate these conditions at the expense of available test times, preventing a comprehensive investigation of unsteady flow processes within the combustor. The proposed facility addresses these issues by relaxing the temperature constraint of the traditional Ludwieg tube (or other purely electrically heated facilities), allowing for longer test times than shock or expansion tunnels, but cleaner flow than arc or vitiation heated facilities and higher temperatures.

This facility extends upon the operational concept of the LICH (Ludwieg Tube with Isentropic Compression) by Oldfield, Schultz, & Jones [11] by preheating the

Ludwieg tube (LT) before the free-piston compression. Figure 1.3 illustrates the components and conceptual operation of the proposed facility. The initial oper-

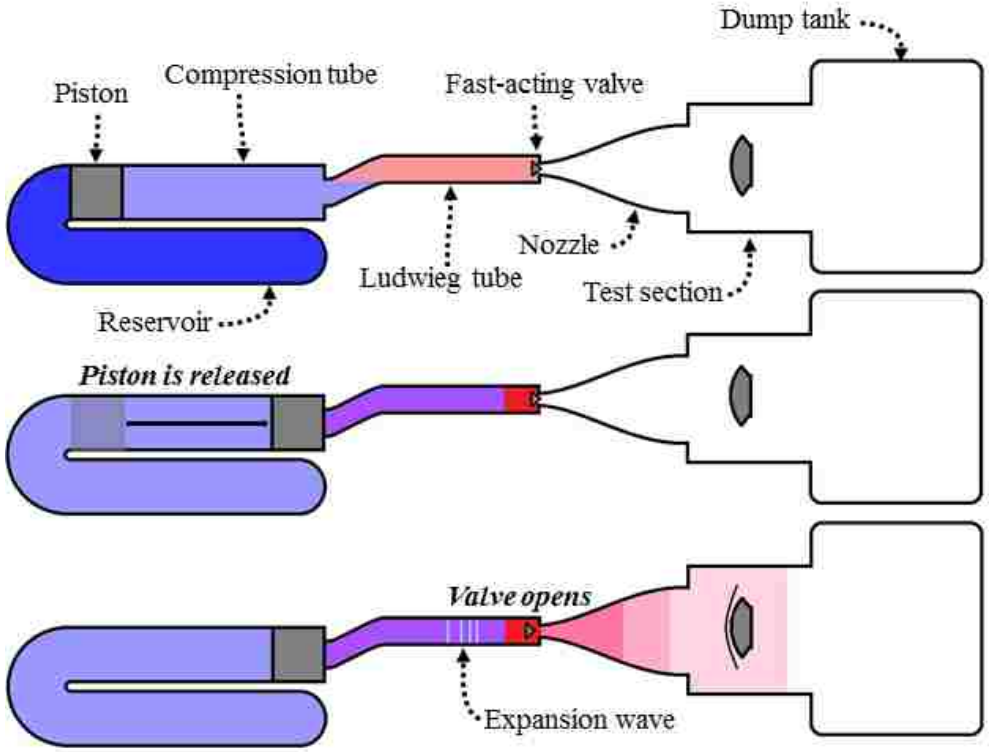

Figure 1.2: Operational concept of the adiabatic-compression preheated Ludwieg tube.

ational state categorizes the facility into pressurized and evacuated components, which are isolated by a closed fast-acting-valve. The major pressurized components include (from left to right in Fig. 1) the secondary reservoir (2R), the compression tube (CT), and the Ludwieg tube (LT). The evacuated components are the nozzle, test section, and dump tank. A free piston is placed between the 2R and CT, while a dog-leg section between the CT and LT is included to mitigate temperature stratification. Provided this radius of curvature is sufficiently large, this dog-leg section is not expected to present any major flow obstruction.

The pressurized components can be further categorized into initially high and low pressure sections. The CT and LT comprise the low pressure section, filled to an initial pressure constrained by the volumetric compression ratio resulting from the piston motion and desired stagnation pressure. The 2R is filled to an initially high pressure state, such that the unconstrained free piston motion is terminated at exactly the end of the CT. The piston motion is prevented until the initial fill pressures reach the desired states and downstream components of the fast-acting-valve are evacuated. Reverse motion of the piston is prevented by directional brakes. Correctly determining this initial 2R fill pressure is critical: the piston must lose all momentum when it reaches the area contraction of the CT to LT while enough pressure is maintained in the 2R for the piston motion to achieve full compression.

The LT is electrically heated before the piston is released, allowing for higher temperatures than would otherwise be available with electrical heating alone. This heated slug of gas (which we refer to as the test slug) in the LT and unheated slug in the CT are both compressed. The large volume ratio of the CT to the LT causes the test slug to occupy a small volume of the LT upon full compression. The expected short time scale of the piston-compression allows for the relaxation of the containing LT material's temperature constraint. The LT material is chosen to be Inconel 601, limiting the maximum initial fill temperature to 900 K. This heating process is similar to the ITAM AT-303 tunnel [12] with two distinct differences which simplify operation: 1. the adiabatic compression process is performed within the unheated section section of the facility and 2. no pressure regulation devices are required to control the piston trajectory after the piston is released.

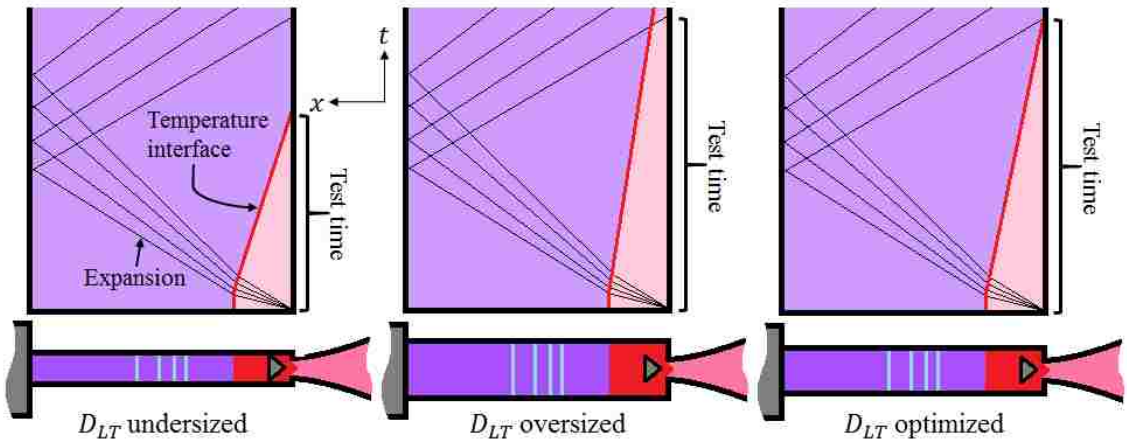

Figure 1.3: Effect of changing the LT diameter, holding the compression ratio, initial LT fill temperature, LT length, and throat size constant.

After the piston motion has terminated, the fast-acting-valve is opened. From this point forward, the facility operates as a conventional Ludwieg tube: the resulting expansion from the valve opening causes the test slug to accelerate through the LT and into the nozzle which accelerates the test slug to the desired supersonic test conditions. Test conditions will be nearly steady until either the hot test slug completely discharges or the expansion reflects off the piston face and reaches the nozzle. We define the optimal operating condition to be when these two events occur simultaneously.

Figure 1.3 illustrates the effect of changing the LT diameter on operating conditions, while constraining the volumetric compression ratio and initial LT fill temperature. The LT diameter is too large if the reflected expansion reaches the nozzle before the test slug completely discharges. A larger LT diameter increases the surface area of heating, thereby increasing heating and manufacturing costs along

with fill times. The size of the CT and 2R must also increase to accommodate the larger LT volume, increasing overall facility size. A LT diameter that is too small causes the test slug to discharge too quickly, which would mean the LT length and overall facility size could be decreased without a performance penalty.

Preliminary numerical results predict the formation of standing waves due to the piston-compression cycle. The strength of these waves are related to the compression time scale. Faster compression cycles are expected to increase the strength of the pressure oscillations. The presence of pressure oscillations induced by a piston compression has been documented in [11]. The source of the oscillations in [11] is the interaction of the compression waves generated by the piston and the rarefaction generated by the valve opening. In the facility described in this work, the valve is opened during the piston motion, before deceleration. The rarefaction in our proposed facility is generated by the deceleration of the piston. The area contraction of the CT to LT is also expected to impact the strength of the oscillations. It is critical to predict the impact the facility geometry and piston mass have on these oscillations, to both constrain the design space and determine methods to mitigate their strength.

1.4 Objectives

The objectives of this work are as follows:

1. Characterize the facility design space under the constraints of the optimal operating condition.

2. Develop a computationally efficient numerical solver to more accurately predict the piston compression trajectory and characterize the available test stagnation conditions.

3. Determine the strength of the standing waves the piston compression cycle induces for a given optimized facility geometry and identify possible mitigation techniques.

Chapter 2: Available Test Times

As noted in chapter 1, the principle difference of the proposed facility from a traditional Ludwieg tube is the presence of a free-piston compression cycle acting on two slugs of air at different temperatures. The test time of a traditional Ludwieg tube scales linearly with the tube's length and the sound speed of the test gas (assuming a weak rarefaction). In our proposed facility, the rarefaction must propagate through two slugs of air at unequal temperatures and volumes. Assuming the optimal operating condition is satisfied, the effective test time is constrained by the arrival of the reflected rarefaction at the nozzle (as is the case in a traditional Ludwieg tube).

This chapter presents the estimation of the expected maximum test times for the facility. The calculations presented here assume the absence of any unsteady pressure oscillations from the piston compression cycle. The valve opening is also assumed to be instantaneous with the resulting rarefaction propagating into a quiescent gas. We first derive an analytical expression for test time as a function of the LT fill temperature, LT length, and desired test stagnation temperature assuming a perfect gas. The second section presents the simplified method of characteristics (MOC) test time estimation, relaxing the finite wave and perfect gas assumptions.

Numerical results presented in the third section (methods presented in chapter 4) agree well with the simplified MOC model.

2.1 Analytical Estimation

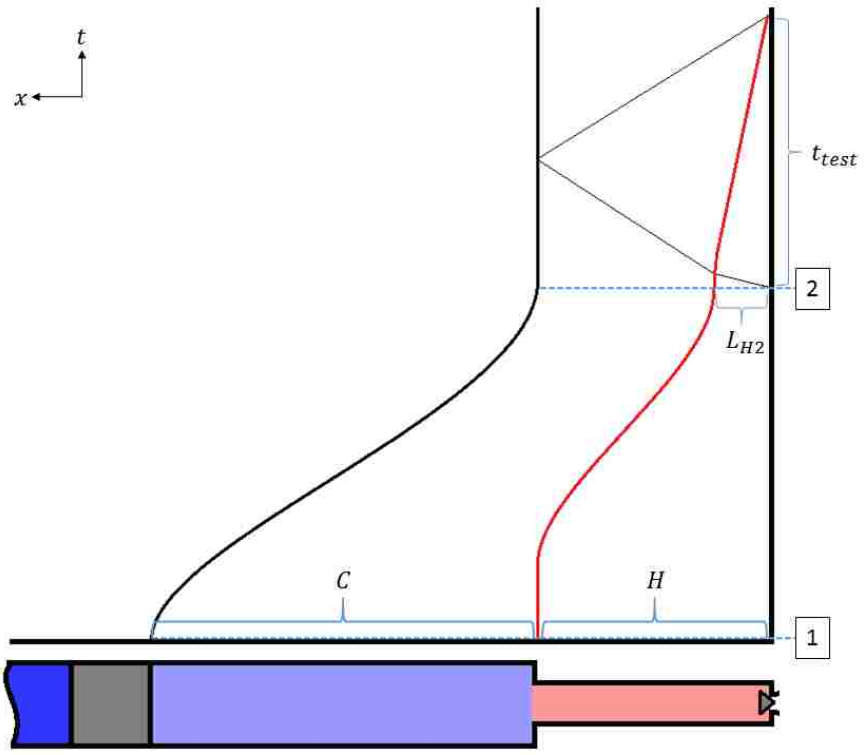

Figure 2.1: x-t diagram of the compression process and valve opening, assuming a single reflection of the rarefaction off the piston face and noncontinuous wave.

The following assumptions are made to simplify the derivation of the analytical expression for test time: 1. the compressed unheated and heated slugs are perfect gasses, with the specific heat ratio remaining constant through compression and across the temperature interface, 2. the gas is quiescent before valve opening, 3.

all waves are finite, 4. the only reflection is at the solid boundary of the piston face, 5. the rarefaction is weak so the temperatures remain constant across the expansion, and 6. the optimal operating condition is satisfied. Figure 2.1 illustrates the simplifying assumptions and denotes the different states of interest. The red line represents the temperature interface separating the cold and hot slugs of gas through the compression and discharge processes. States 1 and 2 (denoted in square boxes on the time axis) represent the initial fill state and final compressed state, respectively. C denotes the cold slug while H denotes the hot slug. First, we define the volumetric compression ratio to be

$$r = \frac{V_1}{V_2} \tag{2.1}$$

where $V_1 = V_{LT} + V_{CT}$ and $V_2 = V_{LT}$. V_{LT} and V_{CT} are the internal volumes of the Ludwieg tube and compression tube, respectively. This definition assumes full compression is achieved. The pressure matching constraint along with the constant specific heat ratio (γ) assumption across the cold and hot slugs allows for the following equality:

$$r = \frac{V_{LT} + V_{CT}}{V_{LT}} = \left(\frac{T_{H2}}{T_{H1}}\right)^{\frac{1}{\gamma-1}} = \left(\frac{T_{C2}}{T_{C1}}\right)^{\frac{1}{\gamma-1}}. \tag{2.2}$$

Here, T_{C1} is the initial temperature of the gas within the CT (it is unheated, so room temperature 300 K), T_{C2} is the compressed temperature of this gas, T_{H1} is the initial LT fill temperature, and T_{H2} is the resulting compressed temperature of the heated gas slug which is also the desired test stagnation temperature. With the temperatures known, we subsequently know the sound speeds of the compressed

slugs which also dictate the rate of propagation for the finite rarefaction. The steady test time can be expressed as

$$t_{test} = \frac{2L_{LT} - L_{H2}}{a_{C2}} + \frac{L_{H2}}{a_{H2}} \tag{2.3}$$

where L_{LT} is the length of the LT, L_{H2} is the length within the LT which compressed test slug occupies, a_{C2} is the speed of sound in the compressed unheated slug, and a_{H2} is the speed of sound in the compressed test slug. The numerator $2L_{LT} - L_{H2}$ defines the distance the rarefaction travels within the unheated slug while L_{H2} is the distance it travels in the heated test slug. From the pressure matching constraint and constant specific heat ratio, L_{H2} is simply given by the compression ratio r. Using equation 2.2 we can make substitutions such that

$$t_{test} = L_{LT}\left[\frac{2 - (T_{H1}/T_{H2})^{\frac{1}{\gamma-1}}}{\sqrt{\gamma R T_{C1}(T_{H2}/T_{H1})}} + \frac{(T_{H1}/T_{H2})^{\frac{1}{\gamma-1}}}{\sqrt{\gamma R T_{H2}}}\right]. \tag{2.4}$$

As expected, it is clear to see in the above formulation that the test time varies linearly with the LT length (under the simplifying assumptions stated). Equation 2.4 also indicates that test time is a monotonically decreasing function of the test stagnation temperature T_{H2} and is monotonically increasing for the initial LT fill temperature. Decreasing the LT fill temperature to test stagnation temperature ratio, T_{H1}/T_{H2}, increases the required compression ratio for the same T_{H2}.

2.2 Simplified Method of Characteristics

Figure 1.3 illustrates a continuous rarefaction with only a single reflection off the piston face. Figure 2.2a illustrates the series of reflections off the cold-hot gas

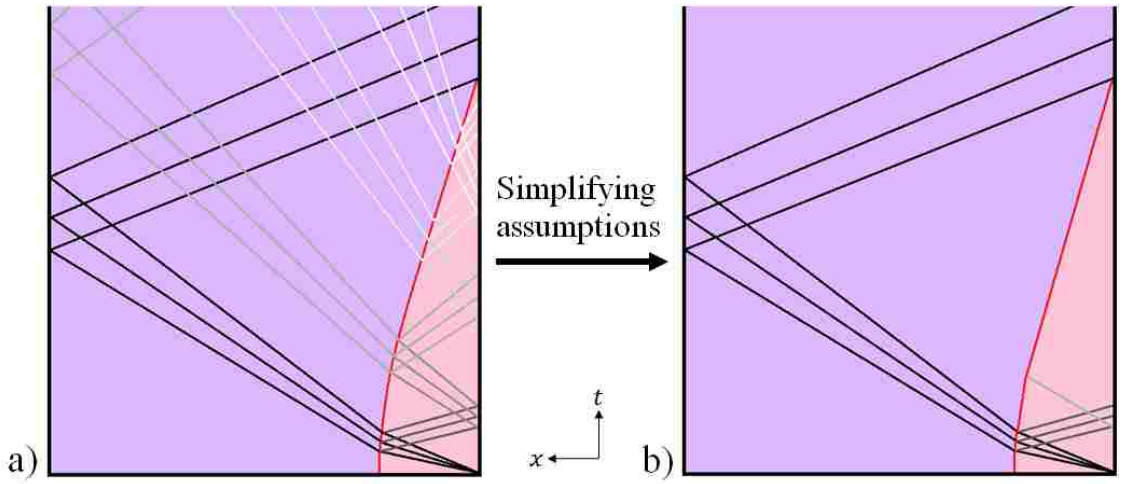

Figure 2.2: a) An illustration of the series of weakening expansions through multiple reflections off the cold-hot gas interface and area contraction at the right boundary. b) Simplifying assumptions are made due to the weakening of these reflected waves.

interface and area contraction to the throat at the right-side boundary. Stagnation conditions change through these reflections as does the contact surface velocity. However, these reflected waves lose strength through the throat opening and at the contact surface. This allows us to make some simplifying assumptions in the method of characteristics (MOC) calculation. This simplified MOC solver is used to determine more accurately the contact surface trajectory and propagation of the strongest rarefaction generated by the valve opening. Figure 2.2b illustrates the simplifying assumptions we use, where only the first reflection through the contact surface and head of the reflected wave from the area contraction are taken into account. MOC (in this application) decouples hyperbolic partial differential equations (PDEs), such as the inviscid gas dynamic conservation laws , into a series of ordinary differential

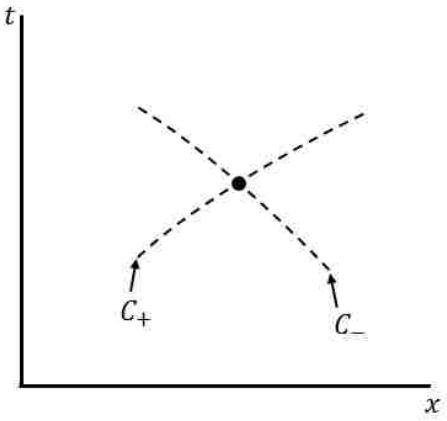

Figure 2.3: Illustration of characteristic lines and their intersection as adapted from [19].

equations (ODEs) along characteristic lines in time and space. Figure 2.3 is an illustration of two characteristic lines of opposite families along which the governing hyperbolic PDEs reduce to ODEs. We use the MOC to investigate further the facility design space in the absence of standing waves from the compression cycle. It is a computationally cheaper alternative when compared to other time-resolved numerical methods while providing a more accurate solution compared to a purely analytical approach.

The Riemann invariants are the integration contants of these ODEs. The unsteady expansions are expected to cause measurable, but weak, variations in the temperature of the cold and hot slugs. This allows us to assume a calorically perfect gas for the MOC analysis. It thus follows from [19], [20], and [21] that the Riemann invariants can be expressed as

$$J_+ = u + \frac{2a}{\gamma - 1}, \quad J_- = u - \frac{2a}{\gamma - 1} \tag{2.5}$$

where u is the fluid velocity, a is the speed of sound, and γ is the specific heat ratio.

The integration constant J_+ holds along the C_+ characteristic while J_- holds along the C_- characteristic. The slopes of the incoming characteristics at each intersection point, as illustrated in figure 2.3, are given by

$$\left.\frac{dt}{dx}\right|_{C_+} = \frac{1}{u+a}, \quad \left.\frac{dt}{dx}\right|_{C_-} = \frac{1}{u-a} \tag{2.6}$$

respectively. The flow upstream of the fast acting valve within the LT remains subsonic, so the C_+ characteristic maintains a positive slope and the C_- characteristic's slope remains negative. The intersection of these incoming characteristics allows us to determine the sound speed and velocity at the intersection location along with the outgoing positive and negative characteristics. The contact surface trajectory is determined by the incoming characteristics along with the velocity and pressure matching constraints for both slugs of gas at the temperature interface.

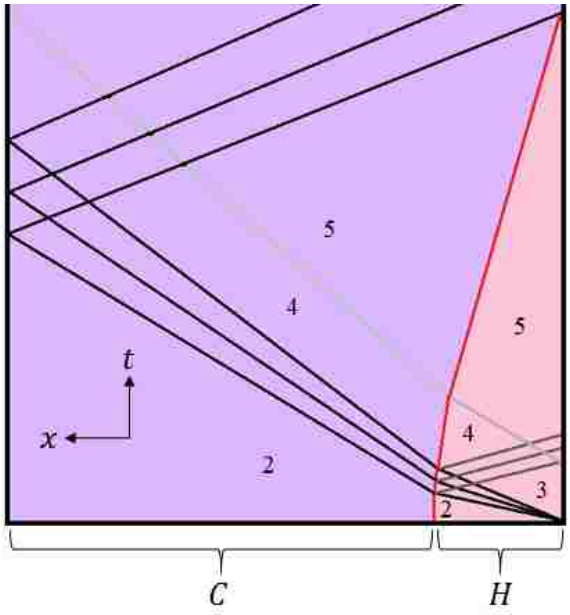

Figure 2.4: Numbered regions used in MOC solver.

As stated earlier, the MOC calculations assume an instantaneous opening of

the valve. The temperature interface is treated as a contact surface separating calorically perfect gasses. The specific heat ratio for each slug is determined using the initial compressed temperature at state 2 in figure 2.1 with equations which follow further in this section.

The stagnation temperature drops through the unsteady expansions, meaning the compression ratio must be adjusted to account for this change. The temperature in region 4 of the hot slug (illustrated in figure 2.4) is used to determine the speed of sound in region 5. The stagnation temperature of region 4 is used to match the required stagnation temperature for the desired test section Mach number at 216.5 K, consistent with a flight altitude of 11 km to 25 km. The Mach numbers in regions 3 and 5 of the hot slug are given by the steady state mass conservation,

$$\frac{A_{LT}}{A_*} = \frac{\rho_* a_*}{(\rho a M)_{LT}} \tag{2.7}$$

where A_{LT}, $(\rho a M)_{LT}$ are the area, density, speed of sound, and Mach number at either of regions 3 or 5 in the LT, and similarly at the throat for A_*, $\rho_* a_* M_*$. The velocity of region 4 is determined by the reflected expansion off the contact surface between regions 4 and 3. The velocity in region 5 is given by the Mach number solution and temperature in region 4. Region 2 in the cold and hot slugs are the states immediately after full compression.

The calorically perfect gas assumption is relaxed for the quasi-one-dimensional relations in the MOC solution. We use the diatomic vibrating gas energy and enthalpy equations to account for the varying specific heat ratio,

$$e(T) = c_{v_p}\left[T + \frac{\theta(\gamma_p - 1)}{\exp\left(\frac{\theta}{T}\right) - 1}\right] \tag{2.8}$$

where c_{v_p} is the constant volume specific heat at 273 K, T is the temperature, θ is $27500 \cdot 9^{-1}$ K, and γ_p is the specific heat ratio at 273 K (1.4). Similarly, the enthalpy for a diatomic thermally perfect gas can be expressed as,

$$h(T) = c_{p_p}\left[T + \frac{\theta(\gamma_p - 1)/\gamma_p}{\exp\left(\frac{\theta}{T}\right) - 1}\right] \tag{2.9}$$

where c_{p_p} is the specific heat at constant pressure for 273 K. These equations are derived from Berthelot's equation of state in [13],

$$p = \frac{\rho RT}{1 - b\rho} - \frac{c\rho^2}{T} \tag{2.10}$$

where b is the molecular size constant and c is the intermolecular force constant. The derivation in [13] uses a first order approximation to 2.10,

$$p = \rho RT\left(1 + b\rho - \frac{c\rho}{RT^2}\right). \tag{2.11}$$

Using these equations, [13] also presents the derivation for the isentropic, thermally perfect flow relations. The compression ratio is given by

$$\frac{v_2}{v_1} = \left(\frac{e^{\theta/T_1} - 1}{e^{\theta/T_2} - 1}\right)\left(\frac{T_2}{T_1}\right)^{\frac{1}{\gamma_p - 1}} \exp\left[\left(\frac{\theta}{T_2}\right)\frac{e^{\theta/T_2}}{e^{\theta/T_2} - 1} - \left(\frac{\theta}{T_1}\right)\frac{e^{\theta/T_1}}{e^{\theta/T_1} - 1}\right] \tag{2.12}$$

where v_1 and v_2 are the specific volumes are two different states. The pressure ratio is given by

$$\frac{p_1}{p_2} = \left(\frac{e^{\theta/T_1} - 1}{e^{\theta/T_2} - 1}\right)\left(\frac{T_2}{T_1}\right)^{\frac{\gamma_p}{\gamma_p - 1}} \exp\left[\left(\frac{\theta}{T_2}\right)\frac{e^{\theta/T_2}}{e^{\theta/T_2} - 1} - \left(\frac{\theta}{T_1}\right)\frac{e^{\theta/T_1}}{e^{\theta/T_1} - 1}\right]. \tag{2.13}$$

These relations are used to determine the state within the Ludwieg tube after compression and the nozzle size relation to the throat. The volumetric compression ratio is nonlinear across both slugs (unlike calorically perfect slugs with matching

specific heat ratios), so the initial and desired final temperature of the test slug is used to determine the pressure ratio. This pressure ratio is then used to implicitly solve for the cold slug temperature after compression. The test slug temperature after compression is chosen so that the stagnation temperature after the unsteady expansions matches the required stagnation temperature for the desired test section Mach number.

2.3 Numerical Verification

The unsteady thermally perfect Euler equations for duct flow are explicitly solved for numerical verification of the MOC solution. The numerical methods used are further detailed in chapter 3.

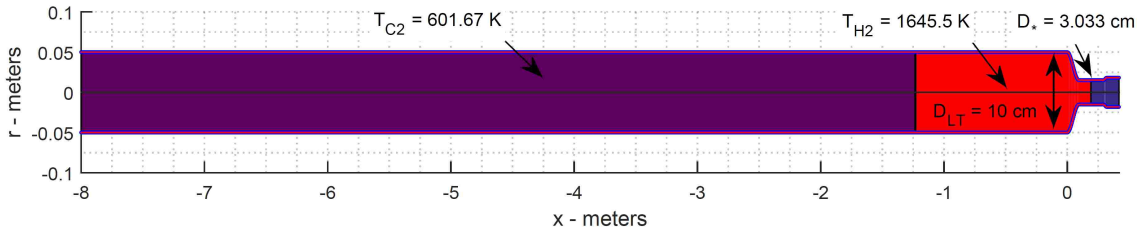

Figure 2.5: Initial conditions for numerical simulation. Notice a convergent section is added between the LT and throat (to the right of x = 0) to prevent instabilities in the simulation. The axes are not scaled proportionally for illustration purposes.

Figure 2.5 shows the initial conditions used in the numerical simulation. An additional convergent section is added between the compression tube and Ludwieg tube to prevent numerical instability from a discontinuous step transition. The full

nozzle is not simulated here to save in computational cost. The diameter of the LT and throat are determined using the MOC solver for an initial fill temperature of 900 K and LT length of 8 meters. The target Mach number here is $M = 6$. An additional divergent section is added after the throat to provide a supersonic outlet, preventing any reflections propagating upstream. Using this geometry and initial conditions determined from the MOC solver, figure 2.6 shows the numerical x-t diagram of the Mach number within the Ludwieg tube. The arrival of the

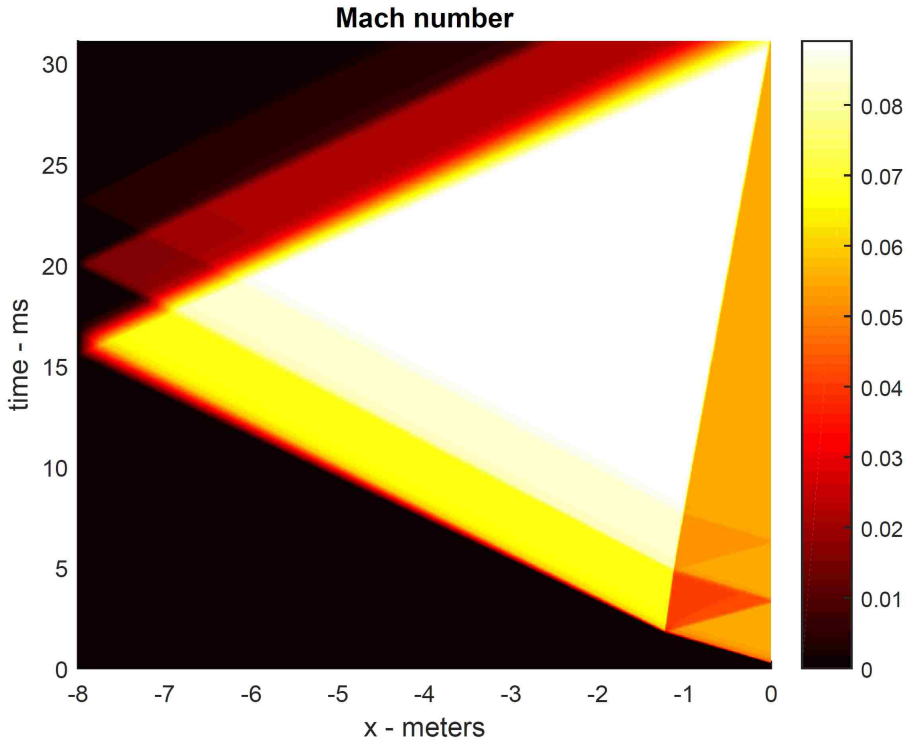

Figure 2.6: A numerical x-t diagram of the Mach number within the Ludwieg tube; here, $\Delta x = 0.004553$ m and $n = 1850$, where n is the number of points in the spatial domain.

temperature interface at the convergent location agrees well with the arrival of the expansion using the initial conditions found from the MOC solver. This is further

illustrated in the plot of Mach number and temperature seen in figure 2.7. A decrease

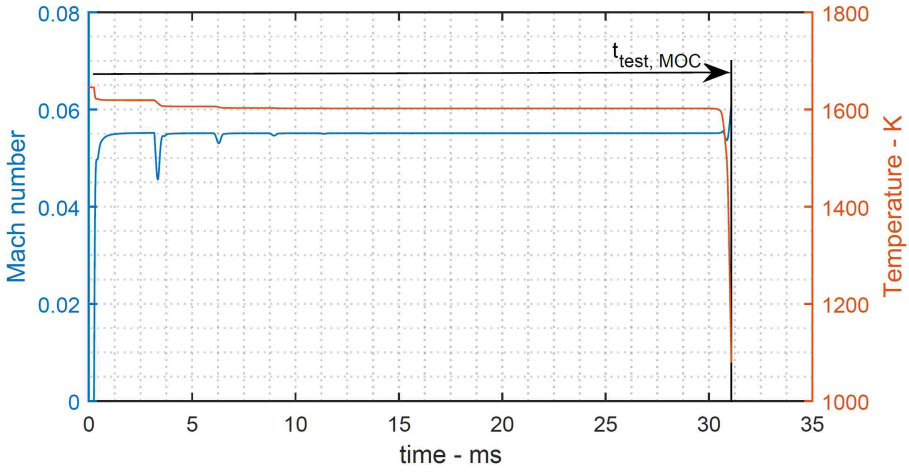

Figure 2.7: Mach number and Temperature time trace at the $x = 0$ location.

in temperature can be seen after the arrival of an unsteady expansion. The first reflection from the temperature interface has the strongest effect. This effect of this unsteady expansion is also seen in the Mach number profile. The conditions are also nearly steady after the first reflection, similar to a traditional Ludwieg tube. Figure 2.8 is a numerical Schlieren demonstrating the propagation of the unsteady waves through the LT. The log of the absolute value of the density gradient is plotted to make the weaker and subsequent waves visible; although these waves are present, they leave no measurable effects beyond the first couple of reflections as seen in figure 2.7.

Another simulation is considered here to demonstrate the agreement between the MOC and numerical solutions. This following case targets a test section Mach number of 5 at 216.5 K with the same initial fill temperature at 900 K. The same grid size is again used. The LT diameter and length remain the same; however, the

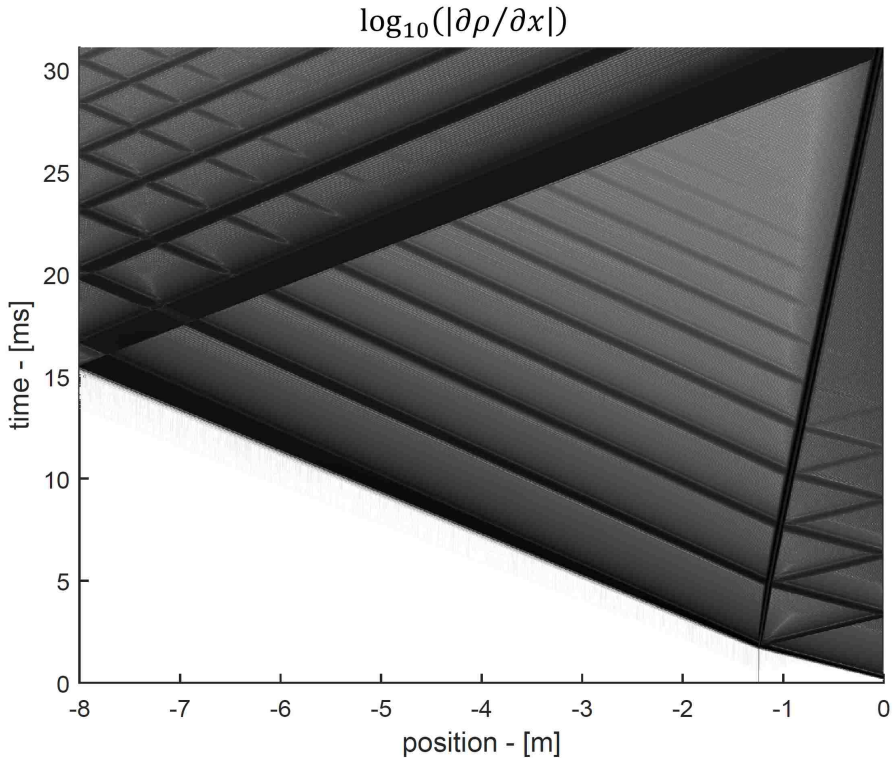

Figure 2.8: Numerical Schlieren illustrating the wave propagation through the system for a test section Mach number of 6.

throat size is now larger to accommodate the larger test slug volume (see figure 2.9). The test slug is larger in this case because a lower Mach number corresponds to a lower stagnation temperature, thereby decreasing the compression ratio required to match the desired test conditions. The results for this case agree well with the MOC solution, as seen in the first case. A larger Mach number is seen in the tube (see figure 2.11), as expected. This case is also a good test for the MOC solver due to the increased strength of the expansion generated by the valve opening. The Schlieren presented for the test section Mach number 5 case (see figure 2.10) captures the qualitative features of the wave interactions. The red lines highlight the strongest features expected and seen in the numerical simulations, that is accounted for in the

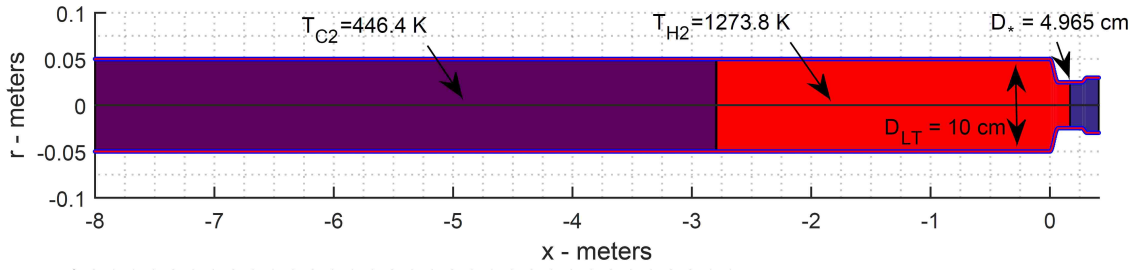

Figure 2.9: Initial conditions for numerical simulation for a test section Mach number of 5.

assumptions of our simplified MOC model. The strength of the expansion wave is expected to decrease for higher compression ratios due to the increasing area ratio between the LT and throat. The next section elaborates on this further.

The trends identified in the two cases here also hold for various various initial conditions. The conclusion is that the simplified MOC model is an acceptable alternative to full numerical simulations for determining ideal sizing constraints.

2.3.1 Results

This section presents the results of the MOC calculations, pertaining to general facility characteristics. Figure 2.12 presents the desired test-section Mach number and its relationship to the available test times, facility volumetric compression ratio, the sizing ratio between the nozzle exit diameter and LT diameter, and also the ratio between the LT and throat. These are determined assuming the optimal operating condition mentioned earlier. The test time and compression ratio results are compared to the analytical results. Here, the analytical compression ratio is determined by the initial fill temperature and stagnation temperature for a given

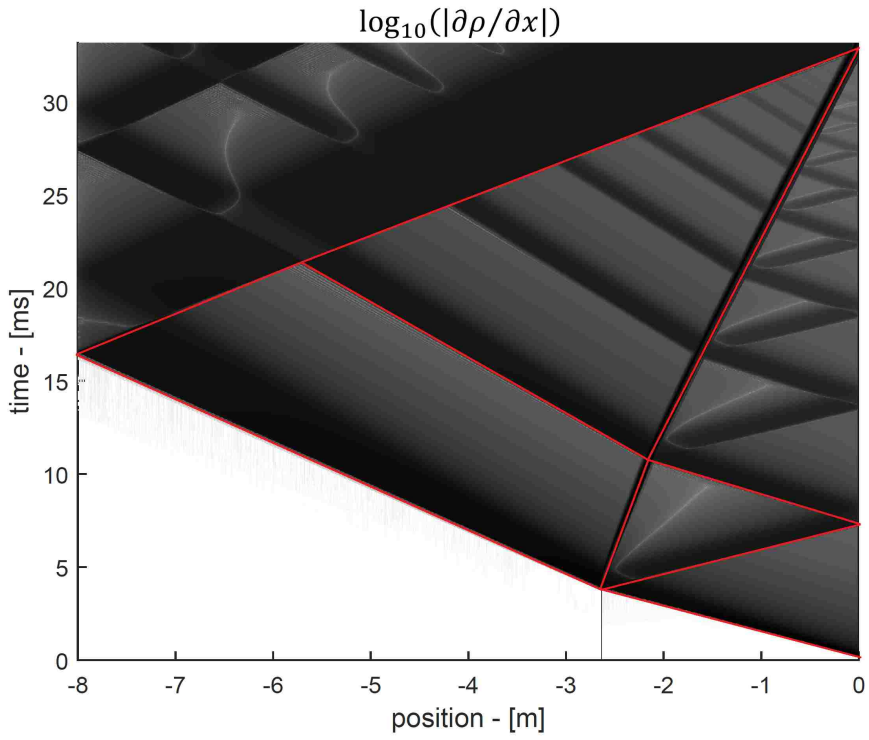

Figure 2.10: Numerical Schlieren illustrating the wave propagation through the system for a test section Mach number of 5. The red lines indicate the important features captured by the simplified MOC analysis.

test section Mach number at 216.5 K, assuming a specific heat ratio of 1.4. The MOC compression ratio is chosen such that the stagnation temperature after the expansions, rather than the temperature immediately after compression, will match the chosen flight Mach number, assuming a free-stream temperature of 216.5 K.

The maximum available test times presented in figure 2.12a demonstrate an inverse relationship with test section Mach number and initial LT fill temperature. This effect is seen in equation 2.4, where an increase in T_{H2}/T_{H1} will decrease the test time. Increasing this temperature ratio requires an increase in the facility's volumetric compression ratio, thereby increasing the temperature (subsequently the

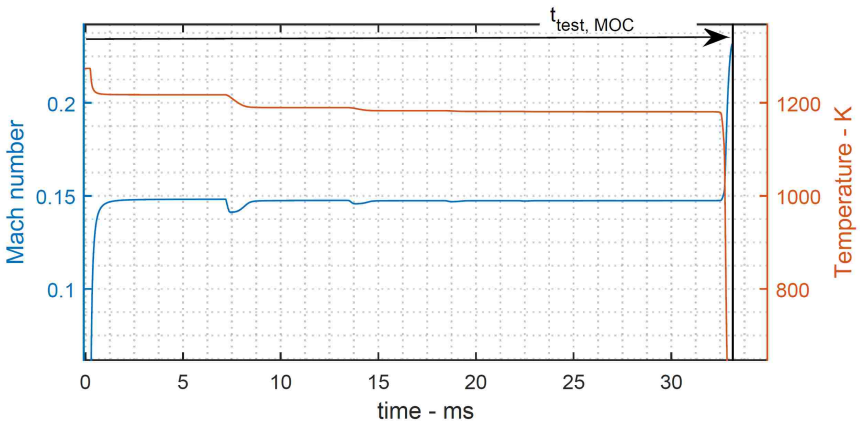

Figure 2.11: Mach number and Temperature time trace at the $x = 0$ location for test section Mach number 5 case.

sound speed) of the unheated gas. An increase in the unheated gas temperature has a more dominant effect on test time rather than the heated test slug itself. This is attributed to the unheated gas occupying a majority of the Ludwieg tube volume. Figure 2.12a also shows the analytical results demonstrate good agreement with the MOC solution over a wide range of test section Mach numbers. This agreement is not as strong in figure 2.12b, where the required compression ratio is predicted to be higher for the real gas MOC solution. This can be attributed to our choice in specific heat ratio. However, adjusting the specific heat ratio such that the analytical compression ratio better matches the thermally perfect gas compression will result in a larger deviation in the test times. Figures 2.12b and 2.12a demonstrate the benefit for a higher initial fill temperature to lower the required facility compression ratio, thereby decreasing overall facility size and increasing available test times (for the same LT length). The test times listed here are 22 ms to 33 ms, and although short, it is still a magnitude of order greater than what is available in shock and

expansion tunnels.

Figure 2.12c shows a decreasing throat diameter for higher test section Mach numbers and lower initial fill temperatures. This sizing relationship is derived from the optimal operating condition. Figures 2.12b and 2.12a demonstrate the acceleration of the rarefaction from increasing compression ratio, but figure 2.12c shows that the decreasing test slug volume for higher compression ratios has the dominant effect on the throat to LT sizing relationship. The throat diameter decreases for increasing compression ratios to slow the discharge rate of the test slug due to its decreasing size. An interesting relationship is seen in figure 2.12d in the nozzle exit to LT diameter ratio for varying test section Mach numbers. For a given initial fill temperature, the variation in nozzle exit to LT diameter ratio is small.

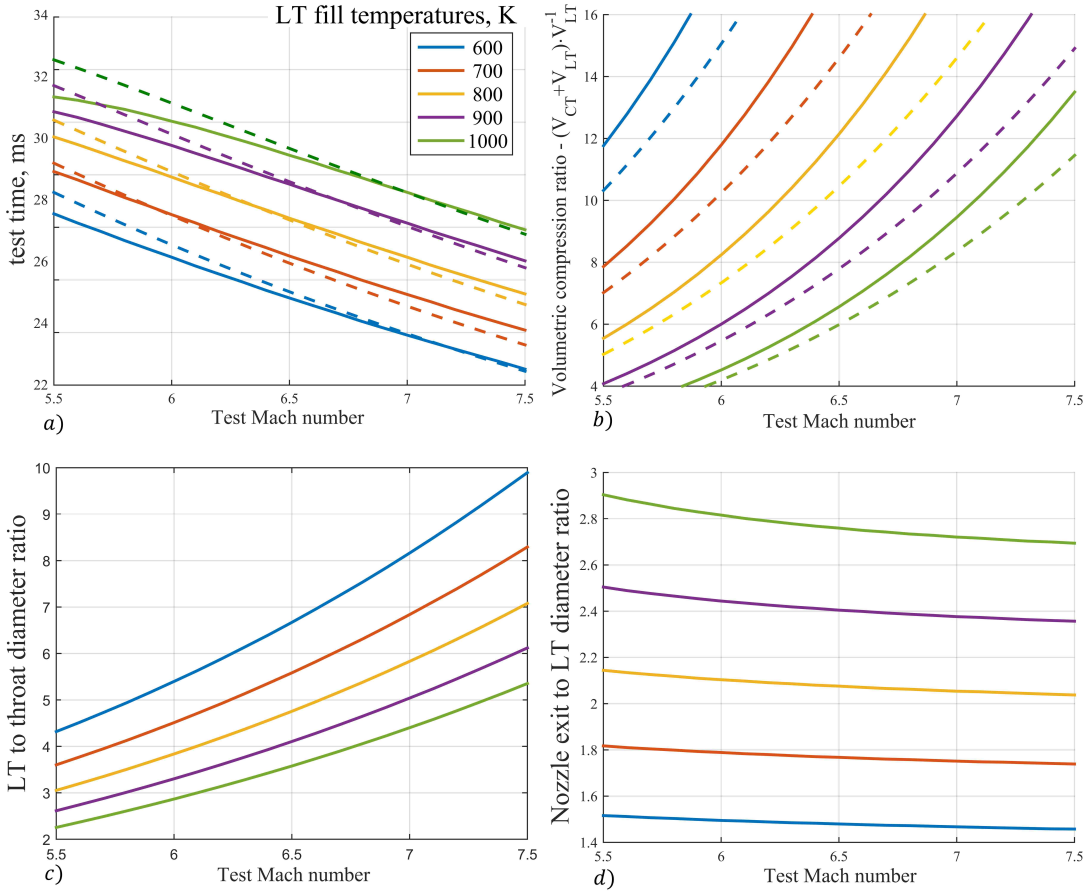

Figure 2.12: MOC results are represented by the solid lines. Analytical results are shown by the dashed lines. All results assume the optimal operating condition is satisfied and an LT length of 8 m. Test section Mach number vs. a) maximum test times, b) nozzle exit to LT diameter ratio, c) volumetric compression ratio, and d) LT to throat diameter ratio.

Chapter 3: Numerical Methods

Analytical solutions have traditionally provided unsatisfactory results [11] for accurately predicting pressure oscillations from an unsteady piston compression cycle. The presence of a step-wise area-contraction between the CT and LT further complicates this issue for our application. As stated in chapter 1, it is imperative to accurately characterize these oscillations to determine methods of mitigation and prevent significant detrimental effects on the test flow quality. It is also critical to determine correct fill pressures to accurately predict piston trajectory. For these reasons, we have implemented a numerical methodology to explicitly solve the unsteady inviscid Euler equations for quasi-one-dimensional duct flow using modern edge reconstruction methods and an approximate Riemann solver. A quasi-one-dimensional formulation is the preferred alternative to more computationally expensive two-dimensional or three-dimensional simulations for the purposes of an extensive design space characterization. Although many physical flow features are not captured, the quasi-one-dimensional formulation is nonetheless a useful tool in predicting the propagation of unsteady waves. This chapter details the methods employed to obtain highly resolved solutions in space and time while mitigating computational costs.

3.1 Previous Quasi-One-Dimensional Facility Modeling

The numerical tool that has traditionally been used to model piston-driven shock-tunnel facilities is known as the quasi-1D Lagrangian code (L1d) [ref]. L1d divides the facility into its separate components such as the compression and shock (in our case, Ludwieg) tubes, and secondary reservoir for the piston driver. Slugs of gas fill these components at their respective initial conditions, and are further divided into a number of smaller control-mass cells. The gas-dynamics of these cells are treated through a Lagrangian framework, with the pressures and velocities at the cell edges estimated through a Riemann solver. The code tracks the trajectory of these cells through the domain along with changes in their state variables. This scheme is second-order accurate in time. Further details on the numerical method are found in [24] and also in [25] as they apply to L1d. L1d treats the stepwise area variations as gradual transitions while engineering correlations are used to account for viscous flow effects, shear stress at the wall, boundary layer mass entrainment, and any losses associated with sudden area changes. A chemical solver is included to account for the nonequilibrium flows that high-enthalpy facilities experience in the reservoir and fast expansion to hypervelocity conditions.

The same year [25] was published, Tani et al. [22] published their application of a fourth-order pointwise non-oscillatory scheme to the piston-driven shock-tunnel. This scheme is applied in the Eulerian frame, solving the inviscid Euler equations by using a non-oscillatory interpolation on the conserved variables to the cell boundaries and then obtaining the flux through an approximate, two-wave-speed Riemann

solver. Their model also incorporates a turbulent heat transfer model for heat loss and an analytical boundary layer model. The code was applied to experimental data from T4 [17] and T5 [5] and was shown to have good agreement, despite the one-dimensional formulation. Predictions of available conditions are not exact, but major flow features are captured with the scheme.

L1d was recently validated [14] by modeling the T-ADFA [15], T3 [16], T4 [17], and HEG [18] piston-driven shock tunnel facilities and comparing the results to the experimental data. Similar to [22], it was able to accurately reproduce the primary shock speeds, piston dynamics, and onset of nozzle supply pressure decay.

Parziale et al. [23] used a standard Roe Riemann solver to perform quasi-one-dimensional Euler computations, characterizing the performance benefits of their proposed vertical expansion tunnel. Their model differs from the previous two mentioned by not incorporating any source terms other than the area variation and also by the absence of a moving boundary which was not necessary for the investigated problem.

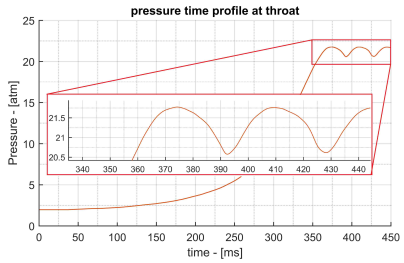

Figure 3.1: Pressure oscillation predicted from the L1d simulation.

The major flow features present in our proposed facility differ from these for which the previous three codes were developed in that the generating flow is free

of shocks and will remain subsonic upstream of the nozzle. L1d has proven to be a valuable design tool and good performance indicator of existing high-enthalpy facilities, and so it was used to perform initial simulations of our proposed facility. The results of a single simulation are presented in figure 3.1. In this particular simulation, the 2R length is 8 meters with a 30 cm diameter, the CT length is 8 meters with a 20 cm diameter, and the LT length is 8 meters with a 9 cm diameter. The piston mass is 100 kg with the 2R fill pressure tailored such that the piston attains zero velocity at the end of the CT. The initial temperature in the LT is 900 K with a fill pressure of 2 bar. Figure 3.1 shows the pressure oscillations as measured at the end of the LT. At higher pressures, the amplitude of the oscillations increases, causing degradation to the flow quality. These simulations were adiabatic and inviscid.

The time scales of the previously mentioned shock-tunnels are limited to a few tens of milliseconds for the compression cycle and a few milliseconds for the test times. The test time of the vertical expansion tunnel of [23] is on the order of a sub-millisecond. Our proposed facility is expected to have a run-time of approximately 30 milliseconds while the compression cycle is on the order of hundreds of milliseconds. An L1d simulation with a grid size of 1300 points with a CFL condition of 0.5 can take up to an hour for such time-scales on a modern personal computer.

The prediction of pressure oscillations by L1d indicate an undesirable flow quality. We develop a different solver to compare solutions with the L1d simulations without resorting to a computationally expensive two or three dimensional model. Excessive run-times can be prohibitive in the solver's usage as an effective

design tool, so higher order methods are used to minimize the grid size for convergence, thereby maximizing the available time step and minimizing simulation run-times. Quasi-one-dimensional simulations have traditionally been a strong predictor of unsteady flow features within these facilities as indicated above, further justifying their use for our application. Furthermore, the full sophistication of a real-gas model provided by L1d is not needed in this application, as the flow is expected to stay below the dissociation regime.

3.2 Governing Equations

The inviscid Euler equations for duct flow are discretized using a finite volume method. Figure 3.2 shows a computational cell for the governing equations,

$$\frac{\partial \vec{U}_i}{\partial t} + \frac{\vec{F}_{i+1/2}A_{i+1/2} - \vec{F}_{i-1/2}A_{i-1/2}}{V_i} = \frac{\vec{S}_i}{V_i} \tag{3.1}$$

where $A_{i\pm1/2}$ is the cross-sectional area at the right and left faces of the cell and V_i is the cell volume. $\vec{U}$ is the vector of conserved variables and $\vec{F}$ is the flux vector,

$$\vec{U} = \left[\rho, \quad \rho u, \quad E\right]^T, \quad \vec{F} = \left[\rho u, \quad p + \rho u^2, \quad u(E+p)\right]^T. \tag{3.2}$$

Here, ρ is the fluid density, u is the velocity, E is the energy as defined by 2.8, and p is the pressure. The source term resulting from the area change for cell i is given by the force balance to be

$$\vec{S}_i = \left[0, \quad p_i(A_{i+1/2} - A_{i-1/2}), \quad 0\right]^T. \tag{3.3}$$

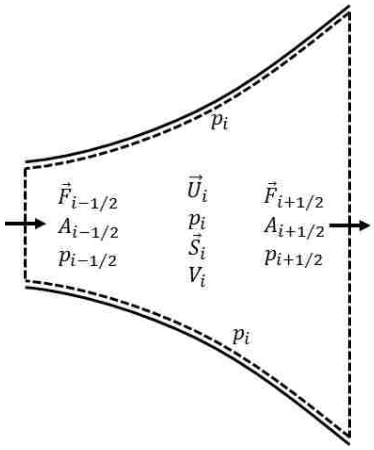

Figure 3.2: A control volume for an ith computational cell.

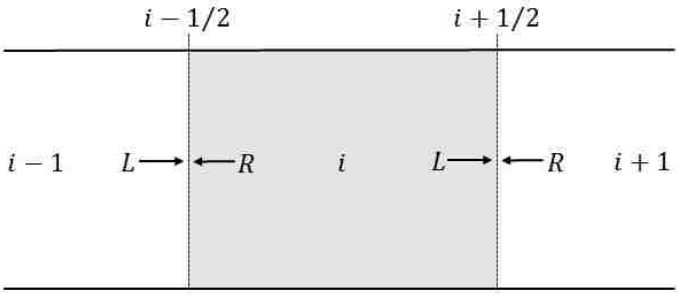

Figure 3.3: Illustration of the edge reconstruction for a cell i.

3.3 Riemann Solver

The flux vector is evaluated at the cell edges using the Harten, Lax, and van Leer with contact restoration (HLLC) Riemann solver introduced by Toro [28]. Edge reconstruction is done on the conserved variables such that

$$\vec{F}_{i\pm1/2} = \vec{F}\big(\vec{U}_{i\pm1/2_L}, \vec{U}_{i\pm1/2_R}\big), \tag{3.4}$$

where $\vec{U}_{i\pm1/2_L}$ and $\vec{U}_{i\pm1/2_R}$ are the reconstructed conserved variables at the left and right sides of the $i \pm 1/2$ cell edges, respectively (see figure 3.3).

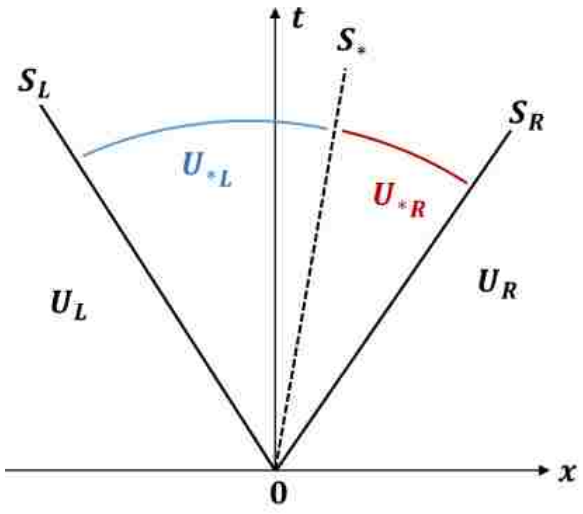

Figure 3.4: Schematic of the HLLC approximate Riemann solver as adapted from Toro [38].

The HLLC Riemann solver approximates the Riemann solution by identifying three wave speeds: the largest wave speed S_R, the smallest wave speed S_L, and the contact wave speed S_* as illustrated in 3.2. The contact wave separates the two intermediate state vectors $\vec{U}_{*_L}$ and $\vec{U}_{*_R}$ bounded by the left and right waves. These intermediate state vectors are used to compute the intermediate fluxes $\vec{F}_{*_L}$ and $\vec{F}_{*_L}$ within these regions. The HLLC numerical flux is defined as

$$\vec{F}^{\text{HLLC}}_{i+1/2} = \begin{cases} \vec{F}_L, & \text{if } 0 \leq S_L \\ \vec{F}_{*L}, & \text{if } S_L \leq 0 \leq S_* \\ \vec{F}_{*R}, & \text{if } S_* \leq 0 \leq S_R \\ \vec{F}_R, & \text{if } 0 \geq S_R \end{cases} \tag{3.5}$$

.

A number of methods exist to estimate the pressure p_* within the intermediate

region and the wave speeds S_L, S_R, and S_*. In the present work, we employ a pressure-based wave speed estimate (proposed by Toro et al. [38]), where an estimate for the pressure p_* is found using the PVRS scheme [29]. The PVRS pressure is defined as

$$p_{pvrs} = \frac{1}{2}(p_L + p_R) - \frac{1}{2}(u_R - u_L)\tilde{\rho}\tilde{a}, \tag{3.6}$$

where the subscripts L and R refer to the left and right states, and $\tilde{\rho}$, $\tilde{a}$ refer to the average density and sound speed of the left and right states. Here, either a geometric mean or a Roe average [30] can be used. We use the Roe averaged values defined as

$$\tilde{u} = \frac{\sqrt{\rho_L}u_L + \sqrt{\rho_R}u_R}{\sqrt{\rho_L} + \sqrt{\rho_R}}, \quad \tilde{H} = \frac{\sqrt{\rho_L}H_L + \sqrt{\rho_R}H_R}{\sqrt{\rho_L} + \sqrt{\rho_R}}, \quad \tilde{\rho} = \sqrt{\rho_L\rho_R}, \tag{3.7}$$

with H as the enthalpy,

$$H = \frac{E + p}{\rho}. \tag{3.8}$$

The average speed of sound is then computed as

$$\tilde{a} = \sqrt{(\gamma - 1)(\tilde{H} - \frac{1}{2}\tilde{u}^2)}. \tag{3.9}$$

The pressure p_* is then given by

$$p_* = max(0, p_{pvrs}), \tag{3.10}$$

which is used to determine

$$q_K = \begin{cases} 1, & \text{if } p_* \leq p_K \\ \left[1 + \frac{\gamma+1}{2\gamma}(\frac{p_*}{p_K} - 1)\right]^{1/2}, & \text{if } p_* > p_K \end{cases} \tag{3.11}$$

where K refers to either the left L or right R states. The wave speeds can then be estimated as

$$S_L = u_L - a_L q_L, \quad S_R = u_R + a_R q_R. \tag{3.12}$$

These wave speed estimations S_K, as suggested by Toro [28], correspond to either the characteristic speed of the head of the rarefaction if the K wave is a rarefaction or an approximation of the shock speed if the wave is a shock. With the right and left state wave speeds known, we then compute the intermediate wave speed

$$S_* = \frac{p_R - p_L + \rho_L u_L(S_L - u_L) - \rho_R u_R(S_R - u_R)}{\rho_L(S_L - u_L) - \rho_R(S_R - u_R)}. \tag{3.13}$$

Knowledge of the different wave speeds allows for the correct flux determination as described in equation 3.5. $\vec{F}_L$ and $\vec{F}_R$ are trivial to find since the right and left states are known. Determining the star region fluxes $\vec{F}_{*K}$ requires finding the star region state variables,

$$\vec{U}_{*K} = \rho_K \left(\frac{S_K - u_K}{S_K - S_*} \right) \begin{bmatrix} 1 \\ S_* \\ \frac{E_K}{\rho_K} + (S_* - u_K)\left[S_* + \frac{p_K}{\rho_K(S_K - u_K)}\right] \end{bmatrix}, \tag{3.14}$$

with the fluxes given as

$$\vec{F}_{*K} = \vec{F}_K + S_K(\vec{U}_{*K} - \vec{U}_K). \tag{3.15}$$

This choice of an intermediate star region state vector allows for a simple addition of multicomponent continuity equations. In practice, we find the different wave speed and pressure estimates of [38] to have negligible impact on the numerical performance for our application. This HLLC Riemann solver has low numerical

dissipation when compared to a Rusanov flux, maintaining high resolution for any discontinuities such as shocks or contact surfaces due to the nature of its wave speed estimations.

3.4 Weighted Essentially Non-Oscillatory Edge Reconstruction

A fifth-order weighted essentially non-oscillatory (WENO) scheme ([26], [27]) is used here for edge reconstruction. This choice is constrained by the moving boundary method further elaborated on in a later section of this chapter. Higher numerical dissipation was observed when using higher order WENO schemes with the chosen moving boundary method, negating the benefits of a higher order scheme.

The WENO schemes are an extension of the essentially non-oscillatory (ENO) scheme introduced by Harten et al. [31] in 1987. Their scheme design uses an adaptive polynomial reconstruction to avoid the Gibbs phenomenon (oscillations that occur due to interpolation across discontinuities: increasing order decreases frequency but peak oscillation amplitude remains constant, moving closer to the discontinuity). The first WENO scheme was introduced by Liu, Oscher, and Chan [27] in 1994 and extended upon the ENO scheme. Their idea was to use a linear combination of multiple, weighted lower order reconstructions to obtain a higher order approximation. Adaptive stencils are used, where more weight is given to stencils containing smooth regions while stencils that contain undesirable oscillations or discontinuities are dropped. Thus, the choice of weights is dependent on the smoothness of the stencils. WENO schemes have been applied extensively to compressible flows. A

further review of its applications can be found in [45] while its derivation is presented in [27]).

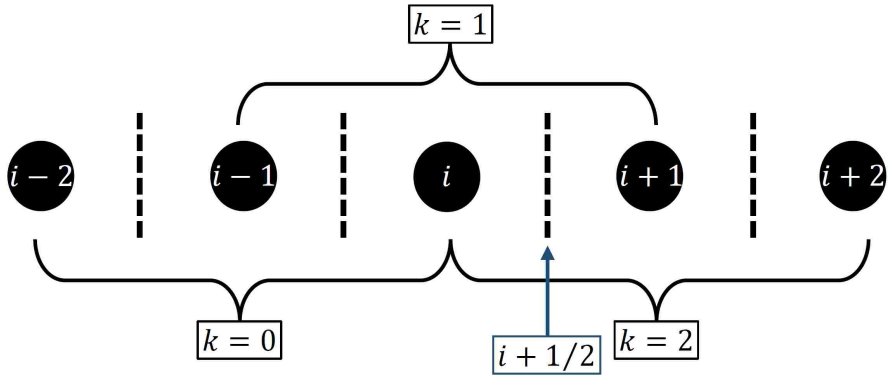

Figure 3.5: Illustration of WENO interpolation stencils for a computational cell i.

The fifth order, three-stencil, three-point WENO interpolation (as used in this work) is given as

$$u_{i+1/2} = \sum_{k=0}^{2} \omega_k u_{k_{i+1/2}}, \tag{3.16}$$

where k indicates the stencil number as illustrated in figure [3.5], $u_{i+1/2}$ is the interpolated variable at the $i + 1/2$ cell edge, and ω_k is the kth WENO weight given to a kth stencil. The WENO weights are calculated as

$$\omega_k = \frac{\alpha_k}{\sum_{l=0}^{2} \alpha_l} \tag{3.17}$$

and here, the choice of α_k (referred to as the unnormalized weights) can vary. Jiang and Shu [26] suggest using

$$\alpha_k = \frac{d_k}{(\beta_k + \varepsilon)^q} \tag{3.18}$$

where d_k are the ideal weights, β_k are the smoothness indicators, ε is a small number to prevent a singularity, and q is an exponent set to 2 in this work as suggested by

Liu et al. [27]. The ideal weights are suggested to be

$$d_0 = \frac{3}{10}, \quad d_1 = \frac{3}{5}, \quad d_2 = \frac{1}{10}. \tag{3.19}$$

The smoothness indicators β_k measure the smoothness of the polynomial approximation $p_k(x)$ of each stencil. The most commonly used is given by

$$\beta_k = \sum_{l-1}^{2} \Delta x^{2l-1} \int_{x_{i-1/2}}^{x_{i+1/2}} \left(\frac{d^l p_k(x)}{dx^l} \right)^2 dx \tag{3.20}$$

and their explicit expressions for stencils $k = 0,\ 1,\ 2$ are

$$\begin{aligned}
\beta_0 &= \tfrac{13}{12}(u_{i-2} - 2u_{i-1} + u_i)^2 + \tfrac{1}{4}(u_{i-1} - 4u_{i-1} + 3u_i)^2 \\
\beta_1 &= \tfrac{13}{12}(u_{i-1} - 2u_i + u_{i+1})^2 + \tfrac{1}{4}(u_{i-1} - u_{i+1})^2 \\
\beta_2 &= \tfrac{13}{12}(u_i - 2u_{i+1} + u_{i+2})^2 + \tfrac{1}{4}(u_{i+2} - 4u_{i+1} + 3u_i)^2.
\end{aligned} \tag{3.21}$$

The three third order interpolations for the given stencils are given by

$$\begin{aligned}
u_{1_{i+1/2}} &= \frac{1}{3}u_{i-2} - \frac{7}{6}u_{i-1} + \frac{11}{6}u_i \\
u_{2_{i+1/2}} &= -\frac{1}{6}u_{i-1} + \frac{5}{6}u_i + \frac{1}{3}u_{i+1} \\
u_{3_{i+1/2}} &= \frac{1}{3}u_i + \frac{5}{6}u_{i+1} - \frac{1}{6}u_{i+2}.
\end{aligned} \tag{3.22}$$

3.4.1 Improved WENO Weights

The above traditional smoothness indicators assign smoothness values to each stencil independent of the other stencils. Borges et al. [46] suggest using new smoothness indicators which take advantage of the entire five point stencil of the 5th order WENO scheme,

$$\beta_k^z = \left(\frac{\beta_k + \varepsilon}{\beta_k + \tau_5 + \varepsilon} \right), \tag{3.23}$$

where

$$\tau_5 = |\beta_0 - \beta_2|. \tag{3.24}$$

β_k and ε are the same as before. Although Borges et al. suggest using a smaller value of ε than previously suggested, we find no measurable difference for our application. Using this new smoothness indicator β_k^z, the unnormalized weights α_k are now defined as

$$\alpha_k = d_k\left(1 + \left(\frac{\tau}{\beta_k + \varepsilon}\right)^q\right), \tag{3.25}$$

where the ideal weights d_k remain the same as previously used. In [46], Borges et al. show that $q = 1$ leads to a 4th order accuracy at critical points in smooth solutions whereas $q = 2$ maintains fifth order accuracy. For this reason $q = 2$ is used in this work.

This choice of improved WENO weights decreases numerical dissipation and increases resolution. This is important when achieving grid convergence, maximizing the allowable cell size and thereby making the CFL condition less prohibitive in computational time.

3.4.2 Relative Limiter

Jiang and Shu [26] comment on the over-aggressiveness of WENO methods in unnecessarily reducing the weights of candidate stencils. Taylor et al. [39] propose a solution to adaptively apply the smoothness measurement such that

$$\beta_k = \begin{cases} 0, & R(\beta) < \alpha_{RL} \\ \beta_k, & \text{otherwise}, \end{cases} \tag{3.26}$$

where

$$R(\beta) = \frac{\max_{0\leq k\leq r}\beta_k}{\varepsilon + \min_{0\leq k\leq r}\beta_k}. \tag{3.27}$$

The smoothness indicators used for this measurement are the standard expressions as shown in equation 3.21. α_{RL} in equation 3.26 is referred to as the relative smoothness limiter which is set to 10 as recommended by Taylor et al. [39].

3.4.3 Slope Limiter

A generic slope limiter [40] is applied to the interpolated variable,

$$u_{i+1/2} = u_i + \frac{1}{2}(u_i - u_{i-1})\phi, \tag{3.28}$$

where ϕ is the slope limiter. The total variation diminishing (TVD) limiter used here is adapted from [41] and is given as

$$\phi_{\text{TVD}} = \max\left[0,\ \min\left(\alpha,\ \alpha\frac{u_{i+1} - u_i}{u_i - u_{i-1}},\ 2\frac{\hat{u}_{i+1/2} - u_i}{u_i - u_{i-1}}\right)\right], \tag{3.29}$$

where $\hat{u}_{i+1/2}$ is the original interpolated variable. As done in [41], α is set to 2.

3.5 Energy Relaxation

The proposed facility will operate at temperatures well beyond the range where calorically perfect state equations are valid. However, the choice of simulating lower hypersonic Mach numbers at a 25 km altitude limits the required stagnation temperature to 1900 K, below the dissociation regime of diatomic nitrogen and oxygen. So to obtain a more accurate prediction of the gasdynamic processes for this temper-

ature regime, the diatomic vibrating gas equations (2.8 and 2.9) are used to model the flow.

Coquel and Perthame [32] introduced a method in 1998 for solving the Euler equations with a more general pressure law for non-perfect fluids. In the same year, Montarnal and Shu [33] published their application of Coquel and Perthame's method to WENO schemes. This method is known as the energy relaxation method. The idea is to decompose the real specific internal energy e into a combination of e_1 and e_2, where e_1 is the energy resulting from the perfect gas pressure law, and e_2 is the difference between e and e_1. This decomposition allows the perturbed difference e_2 to be tracked as an additional term convected by the flow. Coquel and Perthame [32] outline their theory and its application to the Euler equations, while [33] introduces their extension to fifth-order WENO. Here, we outline the relaxed WENO scheme as it applies to the quasi-one-dimensional Euler equations.

Suppose there exists a pressure law such that

$$p = p\big(\rho(x,t), e(x,t)\big). \tag{3.30}$$

where $e(x,t)$ is the energy as determined by equation 2.8, x is the spatial coordinate, and t is the temporal coordinate. The energy decomposition is given as

$$e = e_1 + e_2. \tag{3.31}$$

Coquel and Perthame [32] then define the following as the "consistency relation",

$$p\big(\rho, e_1 + e_2\big) = p_1(\rho, e_1) = (\gamma_1 - 1)\rho e_1, \tag{3.32}$$

where γ_1 is some constant larger than 1. Then, from 3.32 we can define

$$e_1(x,t) = \frac{p\big(\rho(x,t), e(x,t)\big)}{(\gamma_1 - 1)\rho(x,t)} \tag{3.33}$$

$$e_2(x,t) = e(x,t) - e_1(x,t). \tag{3.34}$$

For a given state at time step t_n we have,

$$\rho(x,t_n), \quad u(x,t_n), \quad e(x,t_n), \tag{3.35}$$

and the first step to marching the solution forward to time step t_{n+1} is to apply equations 3.33 and 3.34 to the current n state. The second step is to solve the modified set of Euler equations 3.2, where

$$\vec{U} = [\rho,\ \rho u,\ E_1,\ \rho e_2]^T \tag{3.36}$$

$$\vec{F} = \big[\rho u,\ p_1 + \rho u^2,\ u(E_1 + p),\ \rho u e_2\big]^T, \tag{3.37}$$

and the new source term is,

$$\vec{S_i} = \Big[0, \quad p_i(A_{i+1/2} - A_{i-1/2}), \quad 0, \quad 0\Big]^T. \tag{3.38}$$

Notice that we add only a single continuity equation,

$$\frac{\partial}{\partial t}(\rho e_2) + \frac{\partial}{\partial x}(\rho u e_2) = 0, \tag{3.39}$$

with the perfect gas energy E_1 given as

$$E_1 = \frac{1}{2}\rho u^2 + \rho e_1. \tag{3.40}$$

However, to correctly compute the flux using the HLLC Riemann solver with the additional continuity equation, a slight modification must be made to the intermediate state vector calculation from equation 3.14. Adapting the method described by Toro [38] for multicomponent flows, the new intermediate state vector is now

$$\vec{U}_{*K} = \rho_K \left(\frac{S_K - u_K}{S_K - S_*} \right) \begin{bmatrix} 1 \\ S_* \\ \frac{E_K}{\rho_K} + (S_* - u_K)\left[S_* + \frac{p_K}{\rho_K (S_K - u_K)}\right] \\ e_2 \end{bmatrix}. \tag{3.41}$$

Notice in equation 3.41 that the only term added is e_2; all other calculations remain the same in the Riemann solver.

After solving the system of equations 3.2 with the conserved variables of equation 3.36, flux vector of equation 3.37, and the source term of equation 3.38, we obtain the solution at the t_{n+1-} time step,

$$\rho(x, t_{n+1-}),\ u(x, t_{n+1-}),\ e_1(x, t_{n+1-}),\ e_2(x, t_{n+1-}), \tag{3.42}$$

from which we can compute the solution at the next time step

$$\begin{aligned} \rho(x, t_{n+1}) &= \rho(x, t_{n+1-}) \\ u(x, t_{n+1}) &= u(x, t_{n+1-}) \\ e(x, t_{n+1}) &= e_1(x, t_{n+1-}) + e_2(x, t_{n+1-}). \end{aligned} \tag{3.43}$$

The energy relaxation method allows for the real energy to be conserved by introducing equation 3.39. After the energy is obtained in equation 3.43, we implicitly solve equation 2.8 to obtain the correct pressure and temperature. It is also important to note here that the value of γ_1 is chosen to be 1.41 for this work.

3.6 Characteristic Transformation

Consider the one-dimensional Euler equations for a perfect gas in their quasi-linear form,

$$\frac{\partial \vec{U}}{\partial t} + A\frac{\partial \vec{U}}{\partial x} = 0 \tag{3.44}$$

where A is the flux Jacobian defined as

$$A = \frac{\partial \vec{F}}{\partial \vec{U}}. \tag{3.45}$$

A can either be expressed in terms of the conserved variables,

$$A = \begin{bmatrix} 0 & 1 & 0 \\ -\frac{1}{2}(\gamma-3)\left(\frac{u_2}{u_1}\right)^2 & (3-\gamma)\left(\frac{u_2}{u_1}\right) & \gamma-1 \\ -\frac{\gamma u_2 u_3}{u_1^2} + (\gamma-1)\left(\frac{u_2}{u_1}\right)^3 & \frac{\gamma u_3}{u_1} - \frac{3}{2}(\gamma-1)\left(\frac{u_2}{u_1}\right)^2 & \gamma\left(\frac{u_2}{u_1}\right) \end{bmatrix}, \tag{3.46}$$

where

$$u_1 = \rho, \quad u_2 = \rho u, \quad u_3 = E, \tag{3.47}$$

or in terms of the u and a,

$$A = \begin{bmatrix} 0 & 1 & 0 \\ \frac{1}{2}(\gamma-3)u^2 & (3-\gamma)u & \gamma-1 \\ \frac{1}{2}(\gamma-2)u^3 - \frac{a^2 u}{\gamma-1} & \frac{3-2\gamma}{2}u^2 + \frac{a^2}{\gamma-1} & \gamma u \end{bmatrix}. \tag{3.48}$$

Since equation 3.44 is hyperbolic, the matrix A is diagonalizable and so it follows that

$$X^{-1}AX = \Lambda, \tag{3.49}$$

where Λ is a diagonal matrix with its elements as the eigenvalues of A, X is the matrix of right eigenvectors, and X^{-1} is the matrix of left eigenvectors. The eigenvalues of A are

$$\lambda_1 = u - a, \quad \lambda_2 = u, \quad \lambda = u + a, \tag{3.50}$$

with the right eigenvectors,

$$X = \begin{bmatrix} 1 & 1 & 1 \\ u-a & u & u+a \\ H-ua & \frac{1}{2}u^2 & H+ua \end{bmatrix}. \tag{3.51}$$

Finally, we can transform the conserved variables to characteristic variables,

$$\vec{\alpha} = X^{-1}\vec{U}, \tag{3.52}$$

where $\vec{\alpha}$ is the vector of characteristic variables. Equation 3.44 can then be expressed as

$$\frac{\partial \vec{\alpha}}{\partial t} + \Lambda \frac{\partial \vec{\alpha}}{\partial x} = 0. \tag{3.53}$$

Λ is a diagonal matrix, so it follows that equations 3.53 decouple into independent ODEs. The diagonal values of Λ are also referred to as wave speeds, along which each of the above decoupled ODEs holds true.

In this work, we choose to interpolate the characteristic variables rather than the primitive or conserved variables. This allows for reduced oscillations near discontinuities and boundaries, although at the loss of computational speed. The Roe averaged values of a and u at cell i and $i+1$ (see figure 3.5) are used for the transformation. The transformation matrix X^{-1} is applied to the entire five-point WENO stencil. Only the first three equations of the relaxed WENO system are

transformed. Interpolation for equation 3.39 is done on e_2. Montarnal and Shu [33] show that this partial characteristic decomposition has good agreement with the full decomposition. The slope limiter is applied to the interpolated characteristic variables, before transforming back to the conserved variables.

3.7 Time Integration

This work uses a third order total variation diminishing Runge-Kutta (TVD-RK3) method [35] for explicitly moving the solution forward in time. Once the fluxes and source terms are determined, equation 3.2 simplifies into an ODE. Let L be the operator that is defined as

$$L\big(\vec{U}\big) = \frac{\partial \vec{U}}{\partial t}. \tag{3.54}$$

The TVD-RK3 method for moving a solution at time step t^n to t^{n+1} is then given by

$$\begin{aligned}
\vec{U}^{(1)} &= \vec{U}^n + \Delta t L(\vec{U}^n) \\
\vec{U}^{(2)} &= \frac{3}{4}\vec{U}^n + \frac{1}{4}\vec{U}^{(1)} + \frac{1}{4}\Delta t L(\vec{U}^{(1)}) \\
\vec{U}^{(n+1)} &= \frac{1}{3}\vec{U}^n + \frac{2}{3}\vec{U}^{(2)} + \frac{2}{3}\Delta t L(\vec{U}^{(2)}).
\end{aligned} \tag{3.55}$$

The standard CFL condition dictates the size of Δt,

$$\Delta t = n_{\text{CFL}} \frac{\Delta x}{\max(|\lambda_j|)} \tag{3.56}$$

where λ_j are the wave speeds of the entire domain. We use a CFL number of $n_{\text{CFL}} = 0.5$ unless otherwise stated.

It is important to note the update step for the energy relaxation (equation 3.43)

is done outside of the TVD-RK3 loop to save on computational costs associated with implicitly solving the energy equation.

3.8 Boundary Conditions

The presence of a moving piston in the facility presents a challenge in the numerical modeling. The treatment of boundaries nonaligned with the grid remains a topic of current research interests. One approach is to resize the entire mesh at each time step to align the boundary cell edge with the boundary, imposing costly transformations on the system. After fitting the mesh to the boundary location, questions still remain in determining the ghost-cell values which should impose the moving boundary forcing onto the fluid. Cut-cell methods [36] exist to address the computational costs of body-fitted meshes. The boundary treatment is done locally at the boundary-occupying cell, but the local reduction of cell size can lead to a prohibitive time-step due to the CFL condition. Immersed boundary [37] and penalization [34] methods allow for a constant grid without the detrimental effects of the cut-cell approximations. This gives the benefit of imposing an arbitrary, non-penetrating boundary in a constant, Cartesian grid, but these methods are theoretically less accurate than procedures which use hybrid or full Lagrangian schemes or body-fitted grids. However, the convenience and acceptable accuracy of immersed boundary methods have made them extremely popular in simulations involving complex physical boundaries.

Recently, in 2010, Tan and Shu [42] published their treatment of a boundary

that is unaligned with the Cartesian mesh. It is a third-order accurate method, and although more complex than traditional immersed boundary and penalization methods, it allows for higher-order accuracy with similar computational benefits. In 2011 [44], they extended their scheme to moving boundaries; this is the chosen boundary treatment for the present work. This section further describes the ghost cell filling procedures for the end wall, nozzle outflow, and piston.

3.8.1 Grid Aligned Boundary Treatment

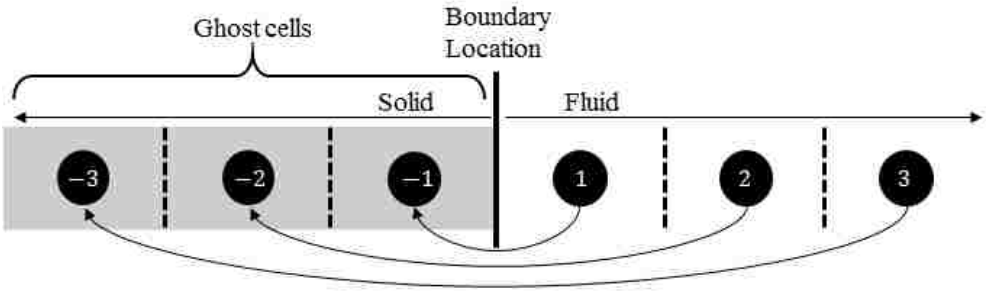

Figure 3.6: Illustration of ghost cell filling procedure for a stationary wall, no penetration condition.

A traditional and popular method of imposing boundary conditions is the ghost cell filling technique. For a stationary wall with the boundary aligned to the cell edge, the reflecting ghost cell filling procedure is illustrated in figure 3.6. The density and pressures are copied over such that

$$\begin{aligned} p_{-1} = p_1,\ p_{-2} = p_2,\ p_{-3} = p_3 \\ \rho_{-1} = \rho_1,\ \rho_{-2} = \rho_2,\ \rho_{-3} = \rho_3. \end{aligned} \tag{3.57}$$

The no-penetration condition of the solid wall is imposed by reflecting the

velocity in the opposite direction,

$$u_{-1} = -u_1,\ u_{-2} = -u_2,\ u_{-3} = -u_3. \tag{3.58}$$

Three cells are used in the filling procedure because the fifth-order WENO scheme requires five points. The left edge, left side interpolation of cell 1 in figure 3.6 requires three points to the left and two points to the right.

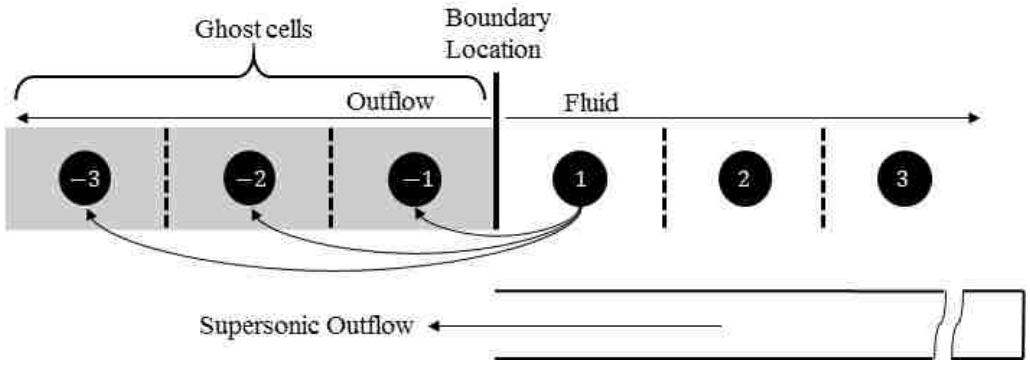

Figure 3.7: Illustration of ghost cell filling procedure for a supersonic outflow.

Figure 3.7 illustrates the ghost cell filling procedure for a supersonic outflow, or a non-reflecting outflow condition. In this case, the outer most cell is copied over to the three ghost cells. This boundary is non-reflecting, so the velocity remains the same direction as in cell 1 for the ghost cells.

3.8.2 Inverse Lax-Wendroff Procedure for Boundary Conditions

Tan and Shu [42] introduced their inverse Lax-Wendroff (IL-W) procedure as a third order accurate treatment of a boundary that arbitrarily intersects a Cartesian grid, and then extended it a year later in 2011 [44] to moving boundaries. In practice, it is a novel ghost cell filling technique that accurately predicts the state of

the boundary occupying cell with no changes to the interior interpolation scheme. This method provides the further benefit of simple extension to higher order interpolations which require large stencils. The principle idea of their scheme is to accurately predict the spatial derivatives at the boundary location to impose ghost cell values using a Taylor expansion. In one dimension, the IL-W procedure takes advantage of available time derivative information in the governing PDEs to obtain this interpolation to the boundary edge of the spatial derivatives. Tan and Shu's numerical examples [44] suggest their method is third-order accurate, with no detriment to numerical stability with standard interior CFL limitations. Here, their one-dimensional scheme is outlined as it applies to the facility model. A further description of their two-dimensional formulation is available at [44].

First, we consider the one-dimensional inviscid Euler equations in their primitive form,

$$\frac{\partial \vec{W}}{\partial t} + A(\vec{W})\frac{\partial \vec{W}}{\partial x} = 0. \tag{3.59}$$

where

$$\vec{W} = \begin{bmatrix} W_1 \\ W_2 \\ W_3 \end{bmatrix} = \begin{bmatrix} \rho \\ u \\ p \end{bmatrix}, \quad A(\vec{W}) = \begin{bmatrix} u & \rho & p \\ 0 & u & 1/\rho \\ 0 & \rho a^2 & u \end{bmatrix}. \tag{3.60}$$

Figure 3.8 illustrates a new cell being uncovered by the movement of the boundary. The number of ghost cells remains the same as the standard ghost cell filling procedure. $i = -3, -2, -1$ are the ghost points, and $i = 0$ is the newly emerging point. $i = 1, 2, 3$ are the cells within the fluid used to construct the ghost cells and newly emerging cell. This newly emerging cell can also be thought of as the cell which

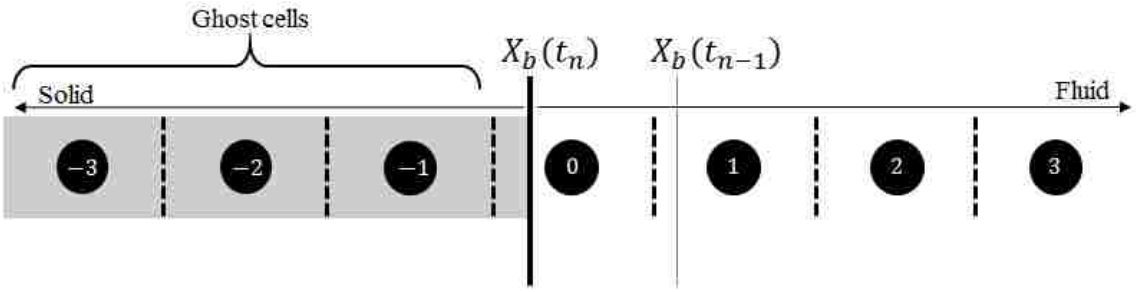

Figure 3.8: Illustration of ghost cell filling procedure for a moving boundary and the newly emerging cell.

the boundary occupies for boundaries moving in the opposite direction. All interior points are updated to the current time step t_n for determining the boundary and ghost cells. The cell values $\vec{W}_i,\ i = -3,\ -2,\ -1,\ 0$ are determined by the Taylor expansion,

$$(W_m)_i = \sum_{k=0}^{2} \frac{(x_i - X_b(t_n))^2}{k!} W_m^{*(k)}, \quad m = 1,\ 2,\ 3, \quad i = -3,\ -2,\ -1,\ 0 \tag{3.61}$$

where $W_m^{*(k)}$ is a $(3-k)$th order approximation of

$$W_m^{*(k)} \approx \left. \frac{\partial^k W_m}{\partial x^k} \right|_{(x=X_b(t_n),\ t=t_n)}. \tag{3.62}$$

The first step in the procedure is to determine the transformation matrix used to map the primitive variables to characteristic space. $A(\vec{W})$ has the same properties as the conservative formulation $A(\vec{U})$, meaning it is diagonalizable. The eigenvalues remain the same as equation 3.50. The primitive variable formulation of the right eigenvectors is

$$K = \begin{bmatrix} \rho & 1 & \rho \\ -a & 0 & a \\ \rho a^2 & 0 & \rho a^2 \end{bmatrix}, \tag{3.63}$$

which also gives us the left eigenvectors,

$$K^{-1} = \begin{bmatrix} l_{1,1} & l_{1,2} & l_{1,3} \\ l_{2,1} & l_{2,2} & l_{2,3} \\ l_{3,1} & l_{2,2} & l_{2,3} \end{bmatrix}. \tag{3.64}$$

The values of cell 1 are used for this transformation matrix in the present work. The Roe averaged values of the i and $i+1$ states introduce increased instability in the solution. Using the left eigenvectors, we obtain the characteristic variables at cells 1, 2, and 3,

$$\vec{V}_i = K^{-1}\vec{W}_i, \quad i = 1, 2, 3, \tag{3.65}$$

from which we use to do either a WENO type extrapolation or a Lagrange polynomial extrapolation to the boundary. In [44], Tan and Shu indicate that a Lagrange polynomial extrapolation should be used if the stencil in front of the boundary is smooth, and otherwise recommend the use of the WENO type extrapolation (introduced in [42], demonstrated to fifth-order in [43]). However, in [43], they suggest only using a WENO extrapolation rather than a Lagrange extrapolation because of the stability issues that may arise. This problem is also seen in our one-dimensional tests. The Lagrange extrapolation for a variable v is given by

$$v^{*(k)} = \left. \frac{d^k p_3(x)}{dx^k} \right|_{x=X_b(t_n)} \tag{3.66}$$

where $p_3(x)$ is a three-point Lagrange polynomial, interpolating the three cells just outside the boundary. The idealized WENO type extrapolation that is suggested for smooth solutions is given by

$$v^{*(k)} = \left. \sum_{r}^{2} d_r \frac{d^k p_r(x)}{dx^k} \right|_{x=X_b(t_n)}, \tag{3.67}$$

where

$$d_1 = \Delta x^2,\ d_2 = \Delta x,\ d_3 = 1 - \Delta x - \Delta x^2. \tag{3.68}$$

$p_r(x)$ are Lagrange polynomials of degree r, which are formulated for three sub-stencils. Δx is the size of each cell in the stencil. This is similar to a traditional fifth-order WENO extrapolation, where three sub-stencils, each consisting of three points, are used. In the extrapolation used here, each sub-stencil increases in size. The candidate sub-stencils here are given by

$$\begin{aligned} S_1 &= [x_1] \\ S_2 &= [x_1,\ x_2] \\ S_3 &= [x_1,\ x_2,\ x_3], \end{aligned} \tag{3.69}$$

and their subsequent Lagrange polynomials are

$$\begin{aligned} p_1(x) &= v_1 \\ p_2(x) &= \frac{v_2 - v_1}{\Delta x} + v_1 \\ p_3(x) &= \frac{v_1 - 2v_2 + v_3}{2\Delta x^2}x^2 + \frac{-3v_1 + 4v_2 - v_3}{2\Delta x}x + v_1. \end{aligned} \quad . \tag{3.70}$$

The weights need to be adjusted for solutions containing discontinuities near the boundary (i.e. shocks) and so this WENO-type extrapolation chooses weights according to their stencil smoothness. This form is similar to the fifth-order WENO interpolation used in the interior scheme. It is given by

$$v^{*(k)} = \sum_r^2 \omega_r \frac{d^k p_r(x)}{dx^k}\bigg|_{x=X_b(t_n)}, \tag{3.71}$$

where ω_r are the nonlinear WENO-type weights. These weights are chosen according to the standard WENO method (see equation 3.17),

$$\omega_r = \frac{\alpha_r}{\sum_{s=0}^2 \alpha_s}, \tag{3.72}$$

and α_r is given by its standard definition,

$$\alpha_r = \frac{d_r}{(\varepsilon + \beta_r)^q}. \tag{3.73}$$

Here, the choice of q can vary. In [42], Tan and Shu suggest using $q = 2$, however in [44] and [43], the authors suggest using $q = 3$. For our one-dimensional application, the choice of this parameter does not produce a meaningful difference in the results. Their more recent suggestion of $q = 3$ is used here in this work along with the suggested value of $\varepsilon = 10^{-6}$. The smoothness indicators used here are given by

$$\begin{aligned}
\beta_1 &= \Delta x^2 \\
\beta_2 &= \sum_{l-1}^{2} \int_{X_b(t_n)}^{X_b(t_n)+\Delta x} \Delta x^{2l-1} \left(\frac{d^l p_2(x)}{dx^l} \right)^2 dx \\
\beta_3 &= \sum_{l-1}^{2} \int_{X_b(t_n)}^{X_b(t_n)+\Delta x} \Delta x^{2l-1} \left(\frac{d^l p_3(x)}{dx^l} \right)^2 dx.
\end{aligned} \tag{3.74}$$

Their explicit expressions are

$$\begin{aligned}
\beta_1 &= \Delta x^2 \\
\beta_2 &= (v_2 - v_1)^2 \\
\beta_3 &= \frac{1}{12}(61v_1^2 + 160v_2^2 + 74v_1v_3 + 25v_3^2 - 196v_2v_1 + 124v_2v_3).
\end{aligned} \tag{3.75}$$

Applying either the WENO-type or Lagrange extrapolation to the characteristic variables, $\vec{V}_i, i = 1, 2, 3$, provides the estimation of the characteristic variable spatial derivatives at the boundary location. This extrapolated kth order spatial derivative at the boundary is herein denoted as $V_m^{*(k)}$ for $k = 0, 1$, and 2.

Obtaining the spatial derivatives of the primitive variables requires a transformation of the extrapolated characteristic derivatives. Here is where we impose the boundary conditions. If the boundary is moving are some velocity $V_b(t_n) = X_b'(t_n)$

at the current time step, then we know that $W_2^{*(0)} = u(X_b(t_n), t_n) = V_b(t_n)$ (recall equation 3.60). This allows us to formulate and solve the following linear system,

$$\begin{bmatrix} 0 & 1 & 0 \\ l_{1,1} & l_{1,2} & l_{1,3} \\ l_{2,1} & l_{2,2} & l_{2,3} \end{bmatrix} \begin{bmatrix} W_1^{*(0)} \\ W_2^{*(0)} \\ W_3^{*(0)} \end{bmatrix} = \begin{bmatrix} V_b(t_n) \\ V_1^{*(0)} \\ V_2^{*(0)} \end{bmatrix} \tag{3.76}$$

where $W_1^{*(0)}$, $W_2^{*(0)}$, and $W_3^{*(0)}$ are the unknowns. To obtain the first order derivatives, Tan and Shu apply their IL-W procedure for the boundary cell velocity. The definition of a material derivative is given by

$$\frac{D}{dt} = \frac{\partial}{\partial t} + u\frac{\partial}{\partial x} \tag{3.77}$$

from which we can rewrite the second equation of the original Euler system (equation 3.59),

$$\frac{Du}{Dt} + \frac{1}{\rho}\frac{\partial p}{\partial x} = 0. \tag{3.78}$$

Here, we can see that Du/Dt is merely the local acceleration in Lagrangian form. First, by isolating the acceleration,

$$\frac{Du}{dt} = -\frac{1}{\rho}\frac{\partial p}{\partial x} \tag{3.79}$$

we can impose the acceleration of the boundary (assuming this is known to us),

$$\frac{Du}{Dt} = V_b'(t_n) = -\frac{1}{\rho}\frac{\partial p}{\partial x}. \tag{3.80}$$

Recall that ρ here is the density at the boundary location (and consequently the boundary occupying cell), which has been determined by solving the first equation 3.76. The same applies to $\partial p/\partial x$ (the spatial derivative of pressure at the boundary

location), and so we can set

$$\frac{\partial p}{\partial x} = \frac{\partial p}{\partial x}\bigg|_{X_b(t_n)} = W_3^{*(1)}, \quad \rho = \rho_{X_b(t_n)} = W_1^{*(0)}. \tag{3.81}$$

This allows us to solve the following system,

$$\begin{bmatrix} 0 & 0 & -1/W_1^{*(0)} \\ l_{1,1} & l_{1,2} & l_{1,3} \\ l_{2,1} & l_{2,2} & l_{2,3} \end{bmatrix} \begin{bmatrix} W_1^{*(1)} \\ W_2^{*(1)} \\ W_3^{*(1)} \end{bmatrix} = \begin{bmatrix} V_b'(t_n) \\ V_1^{*(1)} \\ V_2^{*(1)} \end{bmatrix} \tag{3.82}$$

where $W_m^{*(1)}$ are the unknowns. It is clear to see here that equation 3.80 is recovered from the above system. The algebra for the second order derivatives is tedious and is omitted in [44], but for the sake of completeness the derivation is presented here. The idea is to impose the third order time derivative of the boundary motion into the second order spatial derivative estimation, while also making use of the known derivatives. We again consider the conservation of momentum from the original Euler equations 3.59,

$$\frac{Du}{Dt} = -\frac{1}{\rho}\frac{\partial p}{\partial x} \tag{3.83}$$

then after rearranging and applying the material derivative we obtain

$$\frac{D}{Dt}\left(\rho\frac{Du}{Dt} = -\frac{\partial p}{\partial x}\right). \tag{3.84}$$

Applying the product rule,

$$\frac{D\rho}{Dt}\frac{Du}{Dt} + \rho\frac{D}{Dt}\left(\frac{Du}{Dt}\right) = -\frac{D}{Dt}\left(\frac{\partial p}{\partial x}\right) \tag{3.85}$$

and here, we impose the boundary condition,

$$\frac{D}{Dt}\left(\frac{Du}{Dt}\right) = V_b''(t_n) \tag{3.86}$$

substitute in the first equation of the primitive Euler system 3.59,

$$\frac{D\rho}{Dt} = -\rho\frac{\partial u}{\partial x} \tag{3.87}$$

along with the conservation of momentum (3.83) to obtain

$$\left(-\rho\frac{\partial u}{\partial x}\right)\left(-\frac{1}{\rho}\frac{\partial p}{\partial x}\right) + \rho V_b''(t_n) = -\frac{D}{Dt}\left(\frac{\partial p}{\partial x}\right). \tag{3.88}$$

Expanding the material derivative of the pressure gradient in the third term,

$$\frac{D}{Dt}\left(\frac{\partial p}{\partial x}\right) = \frac{\partial}{\partial t}\left(\frac{\partial p}{\partial x}\right) + u\frac{\partial}{\partial x}\left(\frac{\partial p}{\partial x}\right) \tag{3.89}$$

and then rearranging,

$$\frac{D}{Dt}\left(\frac{\partial p}{\partial x}\right) = \frac{\partial}{\partial x}\left(\frac{\partial p}{\partial t}\right) - u\frac{\partial}{\partial x}\left(\frac{\partial p}{\partial x}\right) \tag{3.90}$$

from which we can factor out $\partial/\partial x$,

$$\frac{D}{Dt}\left(\frac{\partial p}{\partial x}\right) = \frac{\partial}{\partial x}\left(\frac{\partial p}{\partial t} + u\frac{\partial p}{\partial x}\right) - \frac{\partial u}{\partial x}\frac{\partial p}{\partial x} = \frac{\partial}{\partial x}\left(\frac{Dp}{Dt}\right) - \frac{\partial u}{\partial x}\frac{\partial p}{\partial x}. \tag{3.91}$$

Now, we substitute equation 3.91 into equation 3.88,

$$\begin{aligned} \frac{\partial u}{\partial x}\frac{\partial p}{\partial x} + \rho V_b''(t_n) &= -\frac{\partial}{\partial x}\left(\frac{Dp}{Dt}\right) + \frac{\partial u}{\partial x}\frac{\partial p}{\partial x} \\ \rho V_b''(t_n) &= -\frac{\partial}{\partial x}\left(\frac{Dp}{Dt}\right). \end{aligned} \tag{3.92}$$

We once again refer to the original Euler system 3.59,

$$\frac{Dp}{Dt} = -\gamma p\frac{\partial u}{\partial x} \tag{3.93}$$

from which we can substitute into 3.92

$$\begin{aligned} \rho V_b''(t_n) = \frac{\partial}{\partial x}\left(\gamma p\frac{\partial u}{\partial x}\right) &= \gamma\frac{\partial p}{\partial x}\frac{\partial u}{\partial x} + \gamma p\frac{\partial^2 u}{\partial x^2} \\ \gamma p\frac{\partial^2 u}{\partial x^2} &= \rho V_b''(t_n) - \gamma\frac{\partial p}{\partial x}\frac{\partial u}{\partial x}. \end{aligned} \tag{3.94}$$

We now have the second order spatial derivative of velocity, which is a value to be estimated, as a function of the known values of the first order velocity and pressure spatial derivatives. Recalling that

$$W_1^{*(0)} = \rho, \quad W_3^{*(0)} = p, \quad W_2^{*(1)} = \frac{\partial u}{\partial x}, \quad W_3^{*(1)} = \frac{\partial p}{\partial x}, \quad W_2^{*(2)} = \frac{\partial^2 u}{\partial x^2} \tag{3.95}$$

we can formulate and solve the following system for the second order derivatives,

$$\begin{bmatrix} 0 & \gamma W_3^{*(0)} & 0 \\ l_{1,1} & l_{1,2} & l_{1,3} \\ l_{2,1} & l_{2,2} & l_{2,3} \end{bmatrix} \begin{bmatrix} W_1^{*(2)} \\ W_2^{*(2)} \\ W_3^{*(2)} \end{bmatrix} = \begin{bmatrix} W_1^{*(0)} V_b''(t_n) - \gamma W_2^{*(1)} W_3^{*(1)} \\ V_1^{*(2)} \\ V_2^{*(2)} \end{bmatrix}. \tag{3.96}$$

It is clear to see above that equation 3.94 is recovered. To maintain third order accuracy, Tan and Shu [44] suggest updating the boundary occupying cell's velocity by

$$\begin{aligned} u^{(1)} &= V_b(t_n) + \Delta t \left.\frac{\partial u}{\partial t}\right|_{x=X_b(t_n),t=t_n} \\ u^{(2)} &= V_b(t_n) + \frac{1}{2}\Delta t \left.\frac{\partial u}{\partial t}\right|_{x=X_b(t_n),t=t_n} + \frac{1}{4}\Delta t^2 \left.\frac{\partial^2 u}{\partial t^2}\right|_{x=X_b(t_n),t=t_n} \end{aligned} \tag{3.97}$$

where $u^{(1)}$ replaces the $V_b(t_n)$ term (equation 3.76) at the first TVD-RK3 step, and $u^{(2)}$ is at the second step. They use a standard Lax-Wendroff procedure to obtain values for the Eulerian time derivatives, using the spatial derivatives obtained by solving the linear systems 3.76, 3.82, and 3.96. By expanding equation 3.79 and isoluting the Eulerian time derivative we obtain

$$\frac{\partial u}{\partial t} = -u\frac{\partial u}{\partial x} - \frac{1}{\rho}\frac{\partial p}{\partial x} \tag{3.98}$$

and then differentiating with respect to time,

$$\frac{\partial u}{\partial t} = -\frac{\partial u}{\partial t}\frac{\partial u}{\partial x} - u\frac{\partial^2 u}{\partial x \partial t} - \frac{1}{\rho}\frac{\partial^2 p}{\partial x \partial t} + \frac{1}{\rho^2}\frac{\partial p}{\partial x}\frac{\partial \rho}{\partial t}. \tag{3.99}$$

Some of the terms in the above equation are still not known to us, and so we can continue making use of the original Euler system to express the above in known quantities by differentiating equation 3.98 with respect to space,

$$\frac{\partial^2 u}{\partial x \partial t} = -\left(\frac{\partial u}{\partial x}\right)^2 - u\frac{\partial^2 u}{\partial x^2} + \frac{1}{\rho^2}\frac{\partial p}{\partial x}\frac{\partial \rho}{\partial x} - -\frac{1}{\rho}\frac{\partial^2 p}{\partial x^2} \tag{3.100}$$

and then isolating the Eulerian derivative of density from equation 3.87 we have

$$\frac{\partial \rho}{\partial t} = -u\frac{\partial \rho}{\partial x} - \rho\frac{\partial u}{\partial x}. \tag{3.101}$$

Similarly, the Lax-Wendroff procedure is applied to the pressure equation from the original Euler equations and then differentiated with respect to space resulting in

$$\frac{\partial^2 p}{\partial x \partial t} = -(\gamma+1)\frac{\partial p}{\partial x}\frac{\partial u}{\partial x} - \gamma p\frac{\partial^2 u}{\partial x^2} - u\frac{\partial^2 p}{\partial x^2}. \tag{3.102}$$

As a summary, we exploit the information available in the original Euler system by first applying the IL-W method and then use the predicted spatial derivatives in the standard Lax-Wendroff method to more accurately predict the Eulerian terms to maintain third-order accuracy. Tan and Shu [44]also suggest adjusting their IL-W procedure for the first and second TVD-RK3 stages by changing the first equation in the system 3.82. Their suggested change for the first stage is

$$-W_2^{*(0)}W_2^{*(1)} - \frac{1}{W_1^{*(0)}}W_3^{*(1)} = \left.\frac{\partial u}{\partial t}\right|_{x=X_b(t_n),t=t_n} + \Delta t \left.\frac{\partial^2 u}{\partial t^2}\right|_{x=X_b(t_n),t=t_n} \tag{3.103}$$

and the second stage is changed to

$$-W_2^{*(0)}W_2^{*(1)} - \frac{1}{W_1^{*(0)}}W_3^{*(1)} = \left.\frac{\partial u}{\partial t}\right|_{x=X_b(t_n),t=t_n} + \frac{\Delta t}{2} \left.\frac{\partial^2 u}{\partial t^2}\right|_{x=X_b(t_n),t=t_n}. \tag{3.104}$$

So equation 3.82 is replaced by the following in the first and second stages, respectively:

$$\begin{bmatrix} 0 & -W_2^{*(0)} & -1/W_1^{*(0)} \\ l_{1,1} & l_{1,2} & l_{1,3} \\ l_{2,1} & l_{2,2} & l_{2,3} \end{bmatrix} \begin{bmatrix} W_1^{*(1)} \\ W_2^{*(1)} \\ W_3^{*(1)} \end{bmatrix} = \begin{bmatrix} \left.\frac{\partial u}{\partial t}\right|_{X_b(t_n),t_n} + \Delta t \left.\frac{\partial^2 u}{\partial t^2}\right|_{X_b(t_n),t_n} \\ V_1^{*(1)} \\ V_2^{*(1)} \end{bmatrix} \tag{3.105}$$

$$\begin{bmatrix} 0 & -W_2^{*(0)} & -1/W_1^{*(0)} \\ l_{1,1} & l_{1,2} & l_{1,3} \\ l_{2,1} & l_{2,2} & l_{2,3} \end{bmatrix} \begin{bmatrix} W_1^{*(1)} \\ W_2^{*(1)} \\ W_3^{*(1)} \end{bmatrix} = \begin{bmatrix} \left.\frac{\partial u}{\partial t}\right|_{X_b(t_n),t_n} + \frac{\Delta t}{2} \left.\frac{\partial^2 u}{\partial t^2}\right|_{X_b(t_n),t_n} \\ V_1^{*(1)} \\ V_2^{*(1)} \end{bmatrix} \tag{3.106}$$

3.9 Piston Dynamics

The piston dynamics for this work is adapted from L1d. The piston mass is specified by m_p and its area by A_p. The area of the piston is specified by its containing vessel, which in this case is the compression tube. Let d_{CT} be the diameter of the compression tube. Then it follows that

$$A_p = \frac{1}{4}\pi d_{\mathrm{CT}}^2. \tag{3.107}$$

Figure 3.9 illustrates the pressure and friction forces acting on the piston at any given point in time. P_L is the pressure at the left face of the piston, and P_R at the right face. F_f is the frictional force due to the seal near the right face of the piston (piston is moving right). This model is adapted from the piston treatment seen in

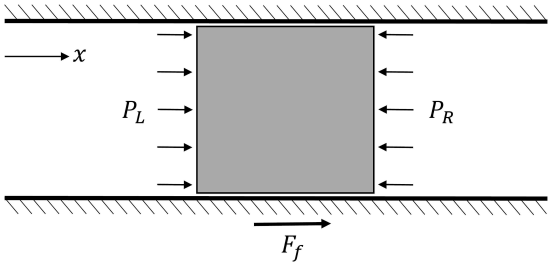

Figure 3.9: Schematic of the friction and pressure forces acting on the piston.

L1d [25]. The maximum friction force is given by

$$|F_f|_{\max} = \mu_f A_{\text{seal}} P_R \tag{3.108}$$

where μ_f is the coefficient of friction of the seal and CT material and A_{seal} is the area of the seal facing the side of piston motion. $\mu_f = 2$ is used in this work, as done in [25]. The seal area used in this work is determined by matching the initial piston acceleration for given initial pressures from the L1d code using the T5 piston parameters. The frictional force applied to the piston is given by

$$F_f = \begin{cases} -\text{sign}\left(V_p(t)\right)|F_f|_{\max} & \text{if } |A_p(P_R - P_L) \geq |F_f|_{\max} \\ -A_p(P_R - P_L) & \text{if } |A_p(P_R - P_L) < |F_f|_{\max} \end{cases} \tag{3.109}$$

The above formulation for friction prevents a frictional force from being applied to the piston unless the pressure force is large enough to cause motion. The resulting equations of motion for the piston are

$$\begin{aligned} \frac{d}{dt}\left(X_p(t)\right) &= V_p(t) \\ \frac{d}{dt}\left(V_p(t)\right) &= \frac{1}{m_p}[A_p(P_L - P_R) + F_f] \end{aligned} \tag{3.110}$$

3.10 Code Algorithm

The general algorithm for determining the initial conditions is as follows:

1. Define the length of the Ludwieg tube, nozzle exit diameter, fill temperature in the Ludwieg tube, length of the compression tube, diameter and length of the secondary reservoir, test Mach number, and fill pressure in the compression side.

2. Use the MOC solver to find the optimized facility geometry in the absence of standing waves. This outputs the compression tube's volume, diameter, Ludwieg tube diameter, and throat diameter.

3. Determine the secondary reservoir fill pressure from the idealized piston trajectory equations.

4. Use the idealized piston equations to estimate the secondary reservoir fill pressure for the optimized piston trajectory.

5. Initialize all variables using the above estimations and begin the simulation.

The algorithm for the Euler solver is as follows:

1. If the time step index is below 500, then constrain the CFL number to 0.002 and suppress the third time derivative of piston position for stability.

2. Fill in all ghost cells, using the reflecting conditions for the end wall and throat (before valve is opened), and the IL-W procedure for the moving piston boundary.

3. Do the WENO interpolation then calculate all fluxes and source terms.

4. Update the time derivative of the conserved variables and proceed with the TVD-RK3 integration.

5. Do the force balance on the piston and update the piston position according to Tan and Shu's [44] suggestion.

6. Outside of the TVD-RK3 integration, update the pressure and temperature with the energy relaxation procedure.

7a. Once the piston stops moving, open the valve at the throat. Here, the CFL number is reduced by a factor of the pressure ratio across the throat. This is done to prevent instability from the strong shock that forms due to the high pressure ratio. Also, α in the slope limiter is set to 1 for the nozzle until the unsteady expansion passes. The initial pressure in the nozzle and test section is assumed to be 100 Pa.

7b. For simulations not involving the valve opening, the iterations continue beyond the piston termination until the time value becomes larger than the specified maximum. Computations behind the piston in the secondary reservoir and compression tube are suppressed due to computational costs.

3.11 Verification

The accuracy of the numerical methodology is assessed by comparing the numerical solutions to known analytical solutions. This section presents the results of

these verification tests.

3.11.1 Shock Tube

The Riemann shock tube is first considered to assess the accuracy of the unsteady solution. The results are presented in figure 3.10. The solid blue lines in figures 3.10b and 3.10c present the MOC and analytical solution, while the red circles present the numerical solution. Figure 3.10a presents the numerical $x - t$ density diagram overlaid with the MOC solution (black lines) and the analytical shock speed (red line). The analytical contact surface trajectory is presented in the dashed red line.

The numerical solution demonstrates strong agreement with the MOC and analytical solution. The contact surface is captured within six cells, while the shock is contained within five cells. The solution also maintains high resolution within the non-simple region of the rarefaction.

3.11.2 Laval Nozzle

The transonic Laval nozzle is considered to verify the source term in equation 3.2. The outlet pressure (specified in figure 3.11) is set to cause a standing shock within the nozzle. The results are presented in figure 3.11. The numerical results agree well with the theoretical solution. The shock location is accurately predicted by the numerical solution, along with the Mach number and pressure profile throughout the nozzle.

3.11.3 Moving Boundary

The numerical moving boundary solution is compared to the MOC and analytical solution for an impulsively started piston moving at 200 m/s. The numerical x-t velocity diagram is presented in figure 3.12a, with the spatial velocity and pressure profiles in figures 3.12b and 3.12c, respectively. Here, the numerical solution agrees well with the MOC solution for the rarefaction and the analytical solution for the induced shock.

3.11.4 Comparison with L1d

A comparison between our numerical methodology and L1d is made. The results are presented in figure 3.13; details on the numerical model can be found in figure 4.1 of chapter four. The comparison presented here shows a 7.8 m long 2R with a 30 cm diameter, 8.4 m long CT with a 20 cm diameter, a 7.8 m long LT with a 9 cm diameter, and a 3 cm throat diameter. The piston mass is 100 kg, with an initial driver pressure of 8.4 bar and driven pressure of 2 bar. The grid size used in L1d is 300 in the 2R, 500 in the CT, 500 in the LT, and 100 in the nozzle. The grid size of our numerical model is 900 with uniform spacing across the entire domain. Upon final compression, the Lagrangian nature of L1d's methodology brings the initial 500 cells of the CT into the LT, increasing the final LT resolution to 1000 points. The effects of viscosity and heat-transfer are ignored in this L1d simulation for a more fair comparison. In both simulations, the throat remains closed and acts as a reflecting end-wall until 450 ms, from which the throat is opened.

The pressure oscillation predicted by L1d is seen in figure 3.13b. As stated before, the strength of this oscillation is expected to increase as the pressure increases. Although the present numerical scheme and L1d show strong agreement on the predicted piston trajectory (see figure 3.13a), the present scheme predicts a higher pressure and temperature, seen in figures 3.13b and 3.13c. This can be attributed to the different equation of states. Despite the small differences, the agreement is good between our Eulerian scheme and L1d's Lagrangian scheme. The significance of this agreement is twofold: 1. the standing waves persist in both a finite-volume Eulerian approach and Lagrangian control-mass approach, indicating further investigation of these waves is warranted and 2. this agreement between the numerical methodology of this work and the more well established L1d code (including the previous verification tests) justifies the use of the present work's scheme for this investigation.

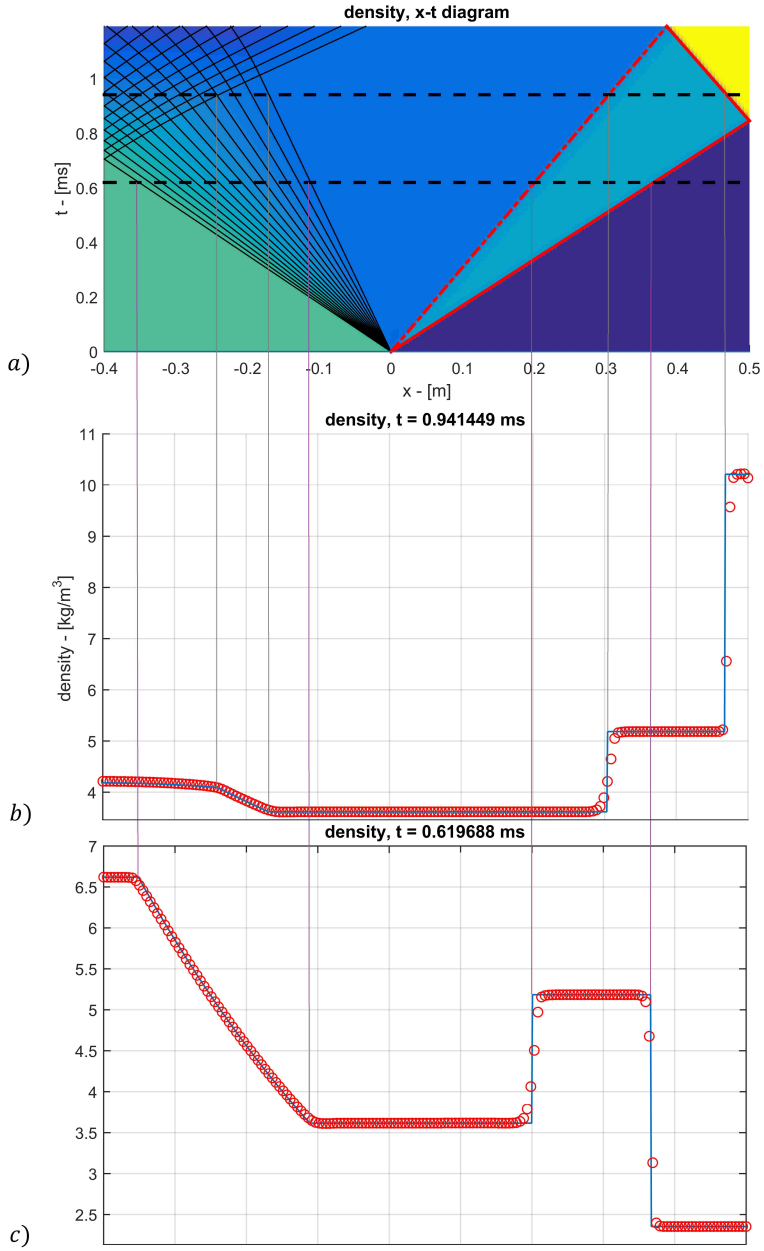

Figure 3.10: This simulation has an initial driver pressure ($x < 0$) of 15 bar with an 800 K temperature, and a driven ($x > 0$) pressure of 2 bar with a 300 K temperature. The grid size is 180 cells with a 0.5 CFL number. a) A numerical $x - t$ diagram of the density. b) The spatial density profile at $t = 0.941449$ ms. c) The spatial density profile at $t = 0.619688$ ms.

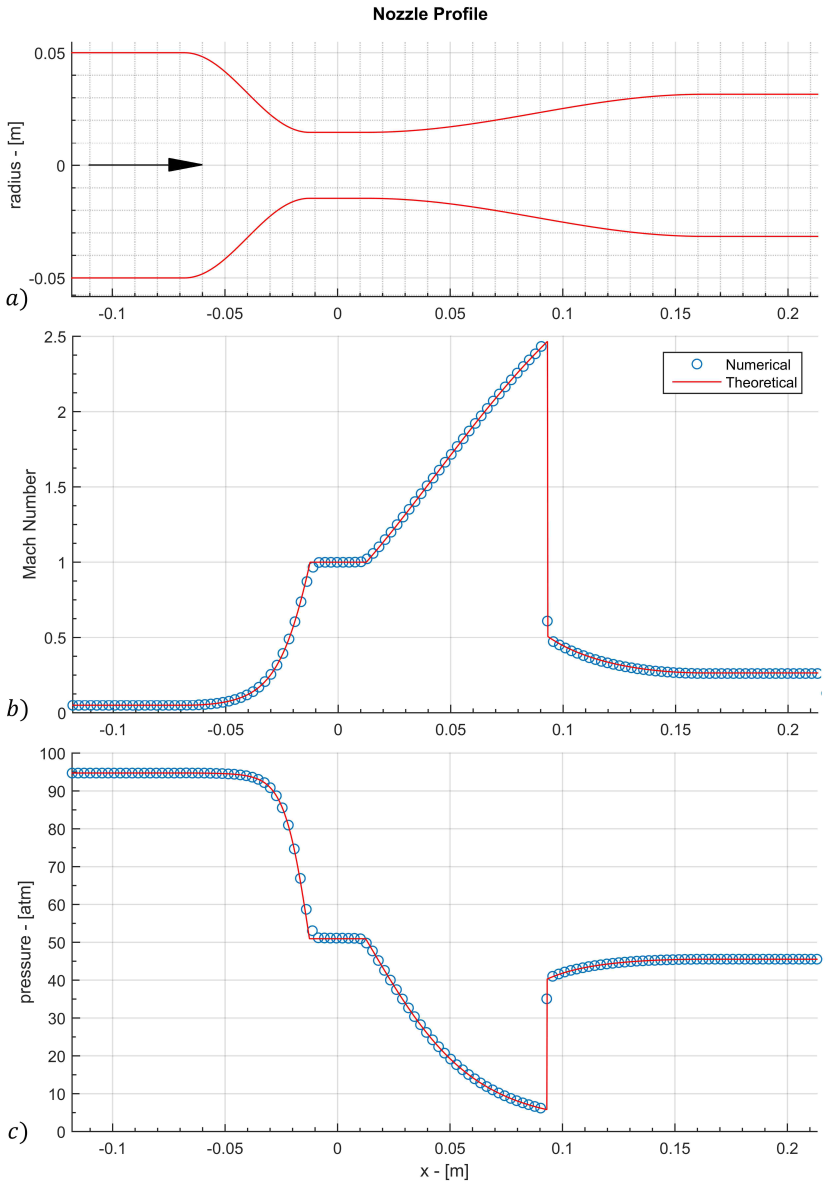

Figure 3.11: The flow is moving left to right. The inlet Mach number is 0.05 with a stagnation pressure of 94.899 atm. The exit pressure is set to 45.5296 atm. The grid size is 125 points. a) The nozzle radial profile as a function of distance. b) The steady-state Mach number profile through the nozzle. c) The steady-state pressure profile through the nozzle.

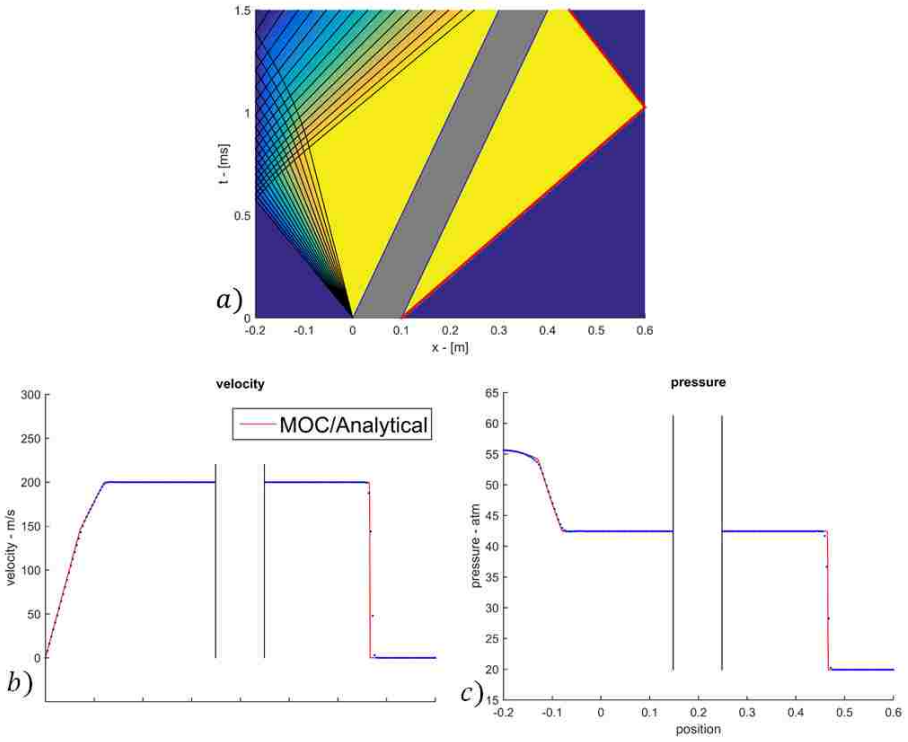

Figure 3.12: The piston is impulsively started and is moving at 200 m/s. a) Numerical x-t velocity diagram, overlaid with the characteristics from the MOC solution (black lines) and the analytical shock solution (red line). The grey region indicates the piston trajectory. b) The spatial velocity profile at $t = 0.75$ ms. The vertical black lines indicate the boundary location. c) The spatial pressure profile at $t = 0.75$ ms.

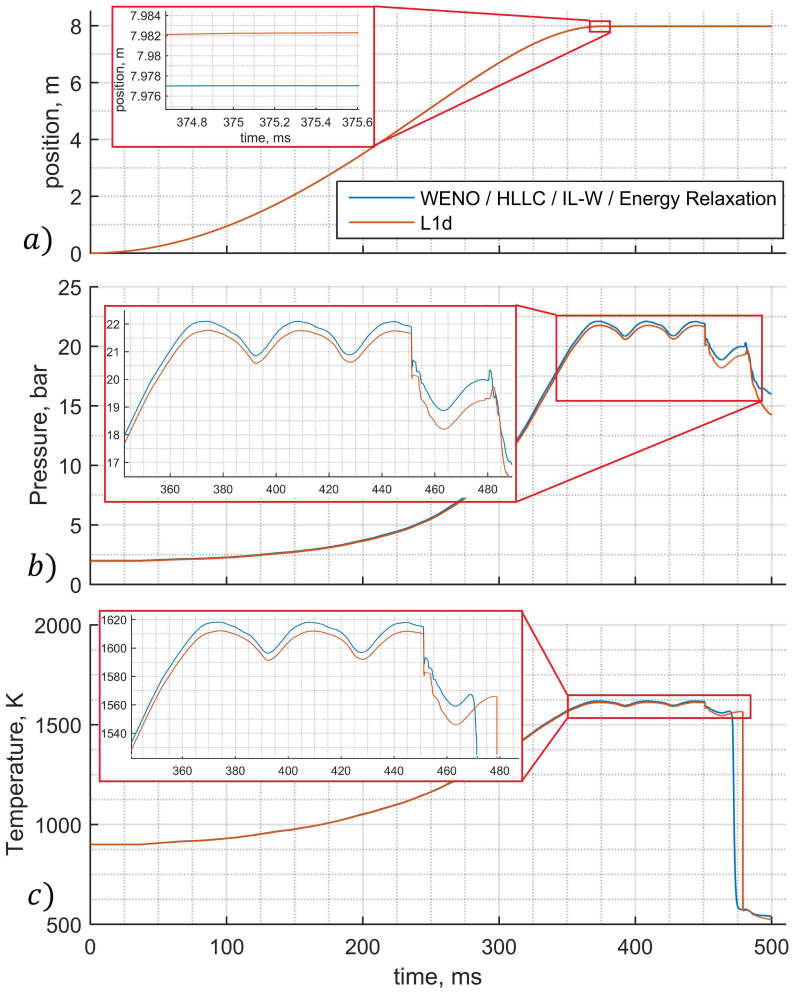

Figure 3.13: Comparison of this work's numerical methodology with L1d using the same geometry. Here, we compare the a) piston trajectory, b) pressure time trace at the LT end, and c) the temperature time trace at the same location.

Chapter 4: Numerical Results

This chapter presents the numerical results for the piston dynamics. The characterization of the resulting pressure oscillations is critical in assessing the performance of the proposed facility. Here, the trends for the oscillation strength over the design space are identified.

4.1 Numerical Model

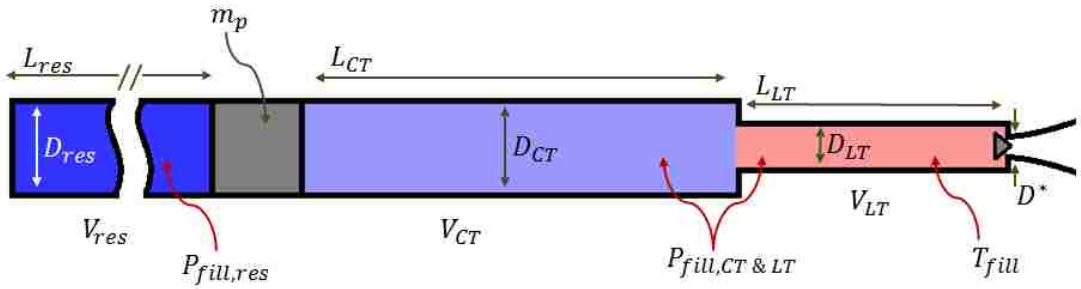

Figure 4.1: Illustration of the linearized tunnel with the variables of interest labeled. Here, L, D, V, and P refer to length, diameter, volume and pressure. The subscripts res, CT, and LT refer to the secondary reservoir, compression tube, and Ludwieg tube. Although illustrated as such here, the compression tube diameter is not necessarily the same as the reservoir diameter.

Figure 1.3 in chapter 1 illustrates the operational concept of the facility, and shows both the dogleg section between the CT and LT, and the reservoir which wraps under the CT to save space. The numerical model brings all the facility components into a linear, inline configuration, further illustrated in figure 4.1. The variables of interest here are the length L, diameter D, volume V, and fill pressures $P_{fill,res}$ and $P_{fill,CTLT}$ of each facility component. The volumes are constrained by the length of the LT and the optimal operating condition for a chosen test Mach number and fill temperature. The optimal operating condition from the MOC calculations are used to determine all LT dimensions and CT volumes investigated in this chapter.

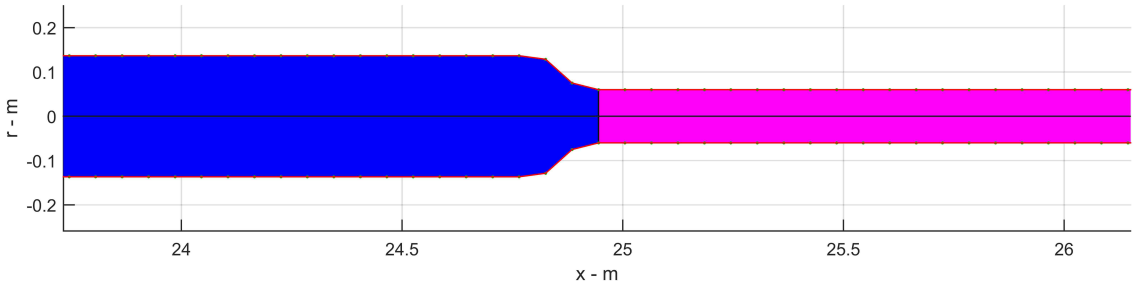

Figure 4.2: Illustration of how the area contractions are modeled. A sine function is used with its minimal slope constrained to 45 degrees. The axes presented here are in proportion. The red region indicates the initial heated state of the Ludwieg tube, while the blue region indicates the non-heated compression tube and area-contraction.

Figure 4.2 shows the extra cells padded between the area contractions to prevent numerical instabilities. A sine function is used to determine the transitional cell radius along the contraction.

4.2 Idealized Piston

The fill pressures are first determined using an idealized model as an initial estimate to the tailored piston trajectory. The tailored piston trajectory is defined as the piston attaining zero velocity at exactly the CT end. The assumptions made here are:

1. All wave speeds are infinite. This means the compression and expansion occurs instantaneously and uniformly across the entire domain for every infinitesimal movement of the piston.

2. The gas is thermally perfect, allowing for the use of the thermally perfect gas equations that were introduced in chapter 2 to more accurately model the compression process.

3. The compression and expansion process is isentropic. There is no heat loss or shock formation due to the piston motion.

Figure 4.3 shows the differences in the piston trajectory prediction when using the idealized model versus the numerical model. The deviation increases when the length of the facility components increase, most likely due to the increased time required for the unsteady waves to fully propagate.

The idealized piston model is used to determine the initial fill pressures for any given reservoir, CT, and LT volumes. The reservoir pressure can be further tailored so the piston reaches full compression for the numerical scheme. The CT and LT fill pressure is constrained by the desired stagnation pressure and compression ratio.

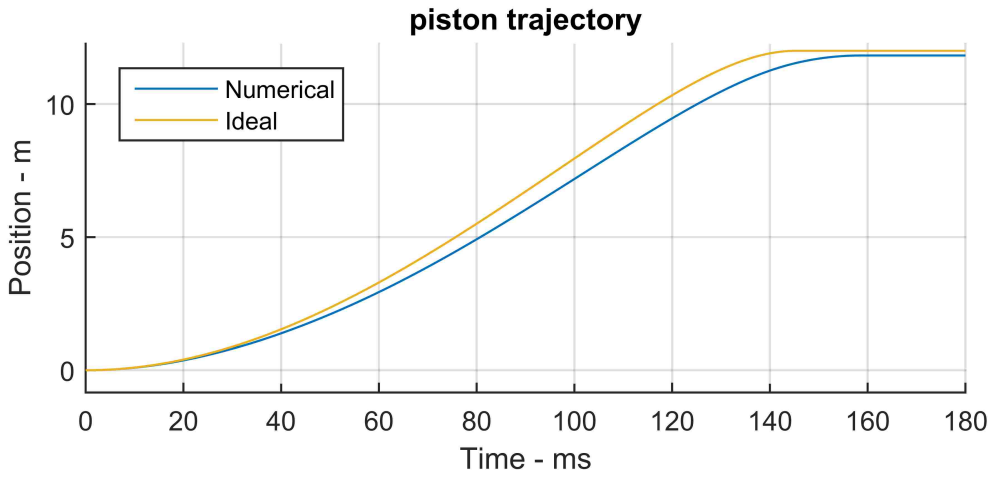

Figure 4.3: Comparison of the idealized and numerical piston trajectory for a targeted compression ratio of 8.78, $m_p = 50$ kg, $L_{CT} = L_{res} = 12$ m, $L_{LT} = 8$ m, and $D_{LT} = 12cm$. The fill pressures are $P_{fill,res} = 20.12$ bar and $P_{fill,CTLT} = 2.994$ bar. Here, the numerical solution comes 18 cm short of the full 12 m trajectory using the same initial conditions of the ideal case.

4.3 Grid Convergence

The grid convergence results are presented in figure 4.4. 950 and 1850 points show higher resolution in predicting the smaller scale oscillations, but for the purposes of this work, which is to identify the larger scale oscillations, 550 points will suffice.

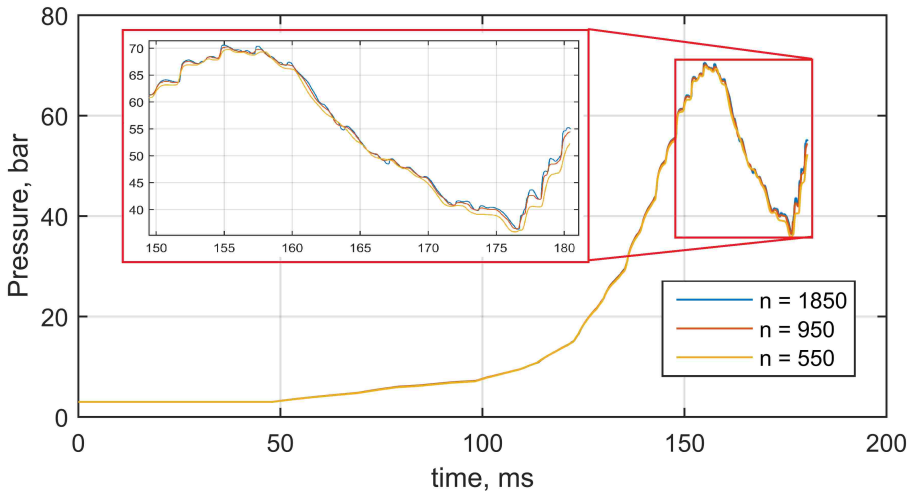

Figure 4.4: Pressure trace at the LT end-wall, just upstream of the throat. The conditions for this simulation are the same as shown in figure 4.3

.

4.4 Pressure Oscillations

The first case presented emphasizes the importance of the numerical modeling and characterizing the highly unsteady flow within the facility. Figure 4.5 demonstrates the "worst case" scenario, where the piston motion induces a shock. This case is for a 50 kg piston mass, 8 m CT, 2R, LT lengths, 12 cm LT diameter, equivalent volumes in the CT and 2R, target stagnation conditions of a 6.5 test section Mach number with a 216.5 K temperature, and beginning with a 900 K LT fill temperature. The CT volume is determined from the MOC solver, assuming optimal operating conditions for the desired test section Mach number and temperature. Initial temperatures in the 2R and CT are 300 K. Major features of the simulation are indicated in figure 4.5. The two most important features to note are the forma-

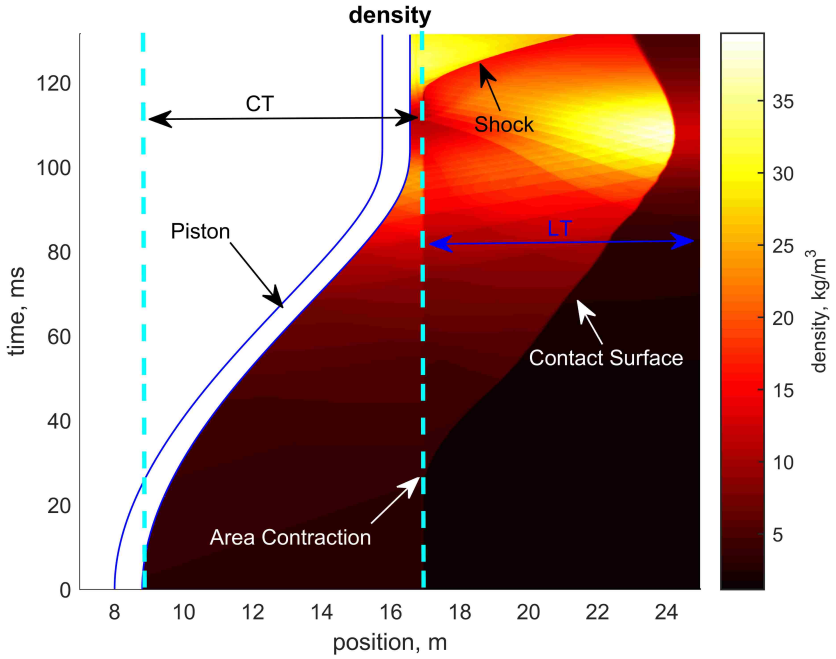

Figure 4.5: Density x-t diagram of $m_p = 50$, $L_{CT} = L_{res} = 8$ m, $V_{res} = V_{CT}$, $T_{fill} = 900$ K, $d_{LT} = 12$ cm, and $d_{CT} = 33.47$ cm. Grid size is 950 cells.

tion of a shock after the piston motion terminates, and the extreme expansion of the test slug. Both will significantly degrade steady test flow quality. The formation of the shock can be attributed to the coalescence of the strong compression waves, generated by the fast compression cycle of the piston. The expansion of the test slug can be attributed to the subsequent deceleration of the piston, which generates an expansion wave. Stronger decelerations are expected to form stronger expansions, further strengthening the expansion of the test slug after piston motion termination. Figure 4.6 is a numerical Schlieren diagram of the same simulation. The expected qualitative wave features of the unsteady flow can be clearly seen in this figure. The head of the initial compression wave accelerates as it propagates into the hotter gas within the LT. A wave reflection occurs due to the area-contraction, which

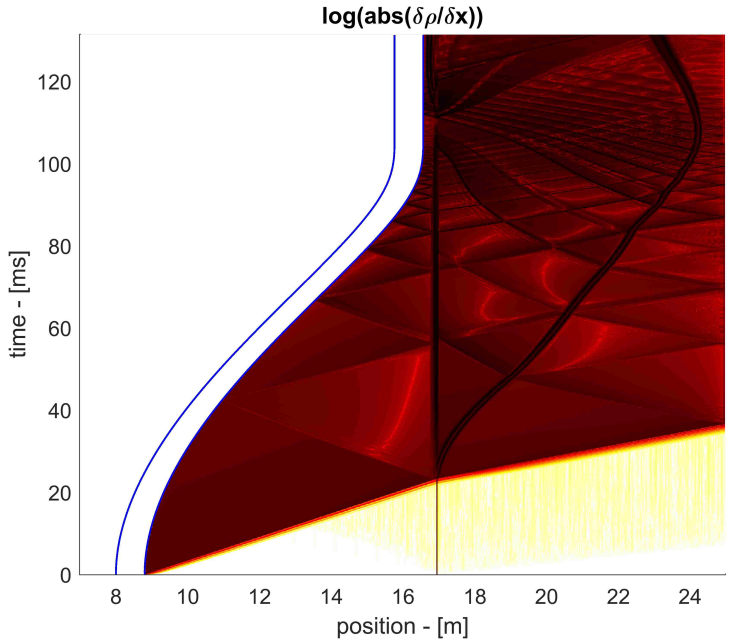

Figure 4.6: Schlieren x-t diagram of $m_p = 50$, $L_{CT} = L_{res} = 8$ m, $V_{res} = V_{CT}$, $T_{fill} = 900$ K, $d_{LT} = 12$ cm, and $d_{CT} = 33.47$ cm. Grid size is 950 cells.

subsequently propagates back to the piston face. The transmitted head of the compression wave reflects from the end wall (the nozzle throat) and propagates towards the temperature interface. This wave then diverges again at the contact surface, where it reflects off the denser, colder gas and also transmits partially into it. The continuation of these reflections can be seen between the piston/area contraction, and the contact surface/LT end wall.

We refer to simple wave theory to better characterize the effects of the unsteady piston-compression, where

$$\Delta v = \frac{\Delta p}{\rho a}. \tag{4.1}$$

Here, v refers to the fluid velocity, p is the pressure, ρ is the density, and a is the speed of sound. The significance of this relation is that a change in velocity can

be related to a corresponding change in pressure for isentropic waves. A larger change in velocity results in a larger change in pressure. This relation suggests the pressure oscillations can be mitigated by minimizing the total change in fluid velocity. In the current framework of the constrained facility design space, the total change in fluid velocity can be mitigated in two ways: 1. a reduction in piston velocity and 2. a reduction in the area contraction ratio between the CT and LT. The maximum piston velocity is a function of the piston mass and the initial fill pressures. Thus, a reduction in piston velocity can be achieved by an increase in piston mass. The area contraction between the CT and LT accelerates the fluid to higher Mach numbers and velocities. Decreasing this contraction ratio is expected to decrease the acceleration of the fluid velocity. To investigate this theory, we parametrically characterize the effects of piston mass and CT lengths on the pressure oscillations, while constraining the compression ratio, initial fill temperature, nozzle throat size, and LT geometry.

Figure 4.7 illustrates the measurement used for determining the strength of the pressure oscillations. The difference of the first peak pressure and first minimum pressure is normalized by the root-mean-square of the pressure between these two points. The CT length and piston mass is varied to characterize their effect on this pressure oscillation. The following simulations constrain the 2R volume and length to the CT volume and length. The initial 2R fill pressure is determined using the ideal theory to minimize computational cost. The LT length is 8 meters, with an initial LT/CT fill pressure of 2.9938 bar.

Figure 4.8 presents the results for varying piston masses of 80 to 200 kg (2.5

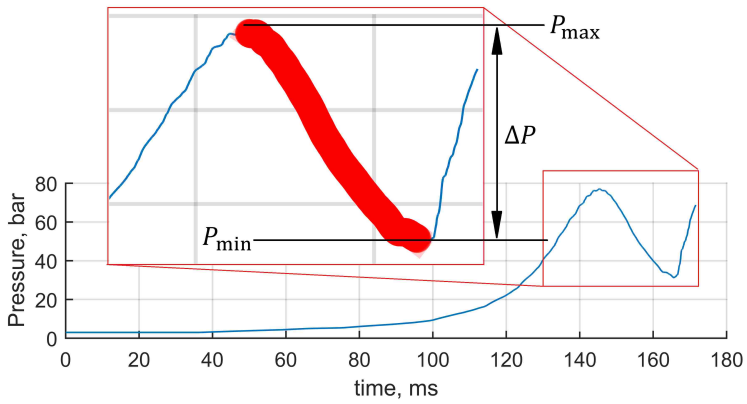

Figure 4.7: Pressure trace at the LT end-wall, just upstream of the throat. The highlighted section goes from the first pressure peak to the second pressure peak, denoted here as P_{max} and P_{min}, respectively. This region is used to calculate the RMS value, which is then used to normalize the total peak-to-peak pressure amplitude ΔP. The simulation presented here has the same parameters as figures 4.5 and 4.6, except here, $m_p = 100$ kg (piston mass is doubled).

kg increments), at different CT lengths of 8 m to 12 m (1 m increments). Longer CT lengths (smaller area contractions), for a given piston mass, result in smaller pressure oscillations. The same is seen for heavier piston masses for a given CT length.

Figure 4.9 plots the pressure oscillations as a function of the maximum velocity seen in the domain. Although the pressure oscillations are more strongly dependent on the peak fluid velocity, a stronger relationship can be seen with the time required to complete the compression in figure 4.10. This suggests that the rate of change of the fluid volume ahead of the piston is a stronger indicator of pressure oscillation

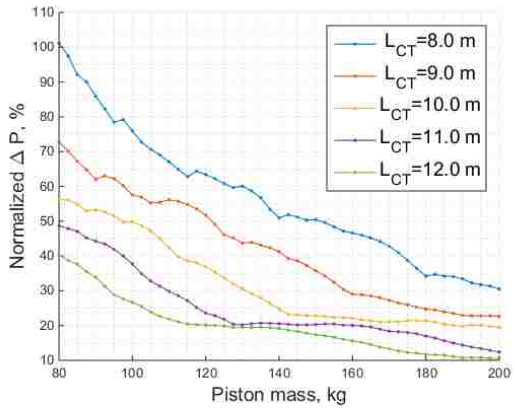

Figure 4.8: Peak to peak pressure oscillation normalized by the RMS value. The CT lengths are varied to change the area contraction ratio while maintaining a constant CT volume. The piston masses are varied from 80 kg to 200 kg in increments of 2.5 kg.

strength.

To decrease the oscillations further, we extend the parametric domain to longer CT lengths of 13 m to 16 m and present the results in figure 4.11. An interesting relationship can be seen here between the oscillation strength and piston mass for any given CT length, where unlike the shorter CT lengths, the longer CT lengths no longer maintain the monotonicity between the piston mass and oscillation strength. We again present the oscillation strength against the compression time cycle in figure 4.12 and see that the agreement is not as strong as the previous shorter CT cases. However, the dependence on the compression time cycle is still stronger than the piston mass. Also, a general trend (although not monotonic) can be seen where longer compression time cycles may result in weaker wave strengths. This loss in monotonicity can be attributed to the constructive and destructive interaction of the

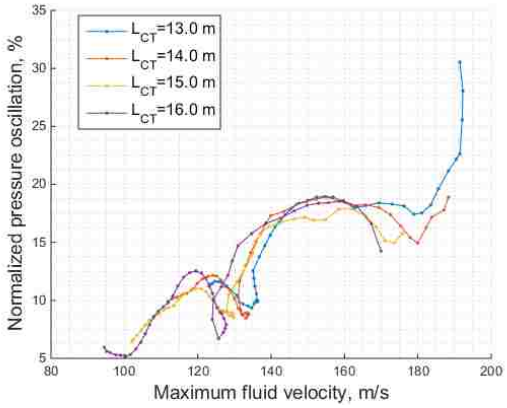

Figure 4.9: Peak to peak pressure oscillation normalized by the RMS value vs. maximum fluid velocity seen in the CT and LT.

unsteady compression and expansion waves. This interaction is highly dependent on whether the interacting waves are right-running or left-running, thereby making the timing of these interactions critical in whether they constructively or destructively interact. This claim has yet to be validated for our specific application.

The results also suggest extremely high piston masses are generally favorable to reducing oscillation strength. It is important to note that higher piston masses are physically unfeasible solutions due to the nature of the tunnel operation. The piston must be removed from the compression tube and moved to its starting point at the beginning of each run. Figure 4.11 also suggests that there might exist diminishing returns in reducing oscillation strength for increasing piston mass. These masses where diminishing returns occur are indicated by circles in figure 4.11. The significance of this result is that although higher masses are generally more favorable to reduce oscillations, lower masses could be used without a significant detrimental effect to the flow quality.

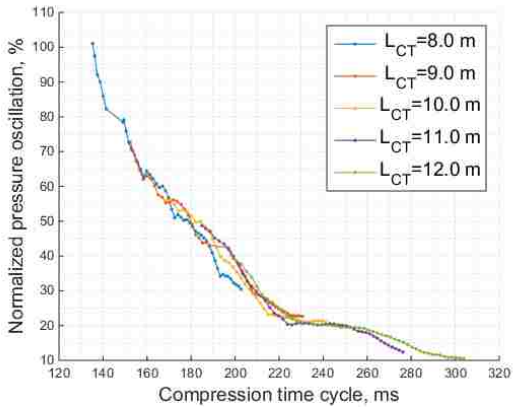

Figure 4.10: Peak to peak pressure oscillation normalized by the RMS value vs. time to complete the compression cycle

4.5 Oscillation Effect on Test Conditions

We quantify the effects of the standing waves on the test conditions for a particular case of a 16 m CT length and 125 kg piston mass. The target conditions are a stagnation pressure of 60 bar and a test section Mach number of 6.5 with a static temperature of 216.5 K.

The pressure and temperature measured at the downstream end of the Ludwieg tube (just upstream of the nozzle throat) are shown in figures 4.13 and 4.14, respectively. The valve is opened soon after the piston motion subsides and on the downward trend of the oscillation cycle. The effect of the wave on test conditions is shown in figures 4.15, 4.16, and 4.17. As seen in figure 4.15, the variation in test section Mach number is small, suggesting the strength of the wave in the Ludwieg tube for the generating flow has minimal unsteady effect. A more significant oscillation in the test section temperature and velocity can be seen in figures 4.16 and 4.17. The

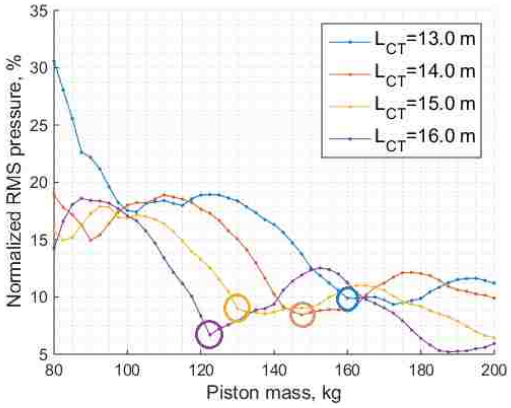

Figure 4.11: Peak to peak pressure oscillation normalized by the RMS value. The CT lengths are varied from 13 m to 16 m. The piston masses are varied from 80 kg to 200 kg in increments of 2.5 kg.

temperature varies by 6 K while the velocity varies by 25 m/s. Although conditions are not exactly constant, it is important to note the strength of the standing waves is most likely exaggerated by the inviscid, one-dimensional nature of the simulation. This suggests the results presented here are extremes, showing the worst-case scenario for tests conditions given this configuration.

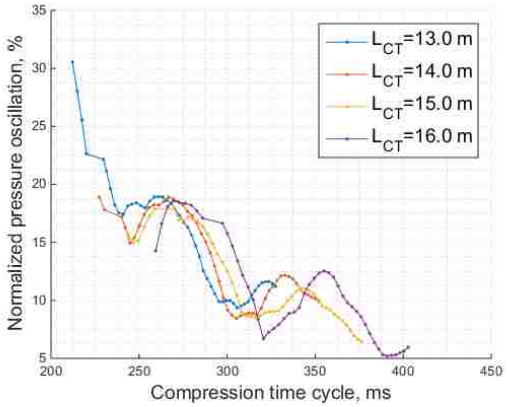

Figure 4.12: Peak to peak pressure oscillation normalized by the RMS value vs. the compression time cycle for longer CT cases.

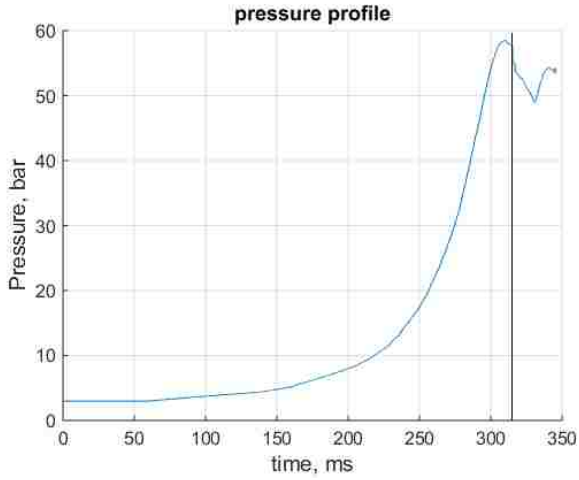

Figure 4.13: Ludwieg pressure vs. time. The valve opening time is indicated by the black vertical line.

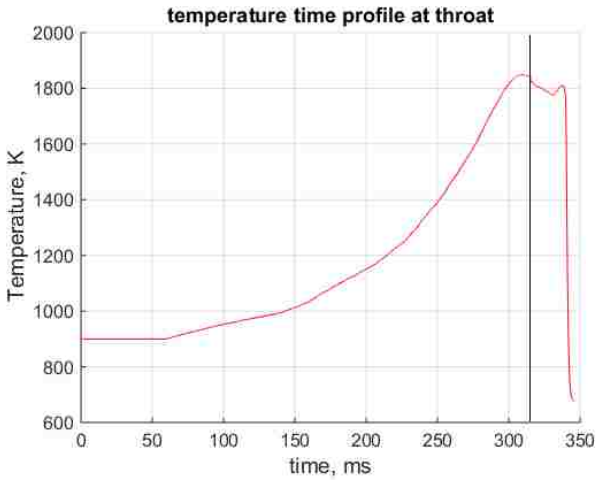

Figure 4.14: Ludwieg temperature vs. time. The valve opening time is indicated by the black vertical line.

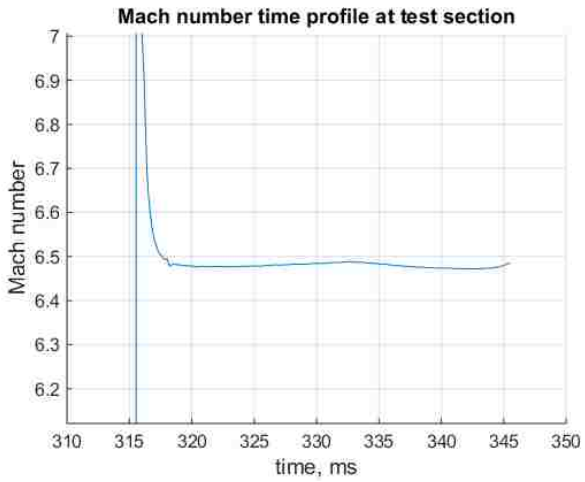

Figure 4.15: Test section Mach number vs. time, after valve opening.

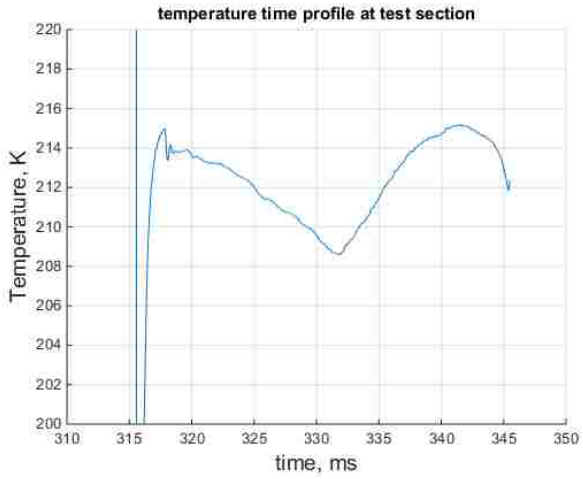

Figure 4.16: Test section temperature vs. time, after valve opening.

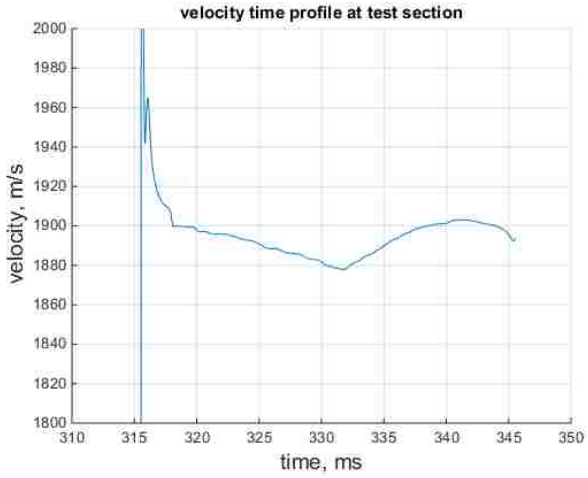

Figure 4.17: Test section velocity vs. time, after valve opening.

Chapter 5: Conclusions and Future Work

5.1 Summary of Results

In this work, the design space and available test conditions of a proposed hypersonic facility have been characterized. A simplified, unsteady method of characteristics solver was used (under the optimal operating condition) to determine the relationship between the Ludwieg tube and nozzle exit diameters and the available maximum test times. These solutions are verified by solving the unsteady Euler equations for duct flow. The expected test times, for an 8 m Ludwieg tube length, range from 33 ms to 23 ms. Higher initial fill temperatures in the Ludwieg tube result in longer steady test times, while an increase on the stagnation temperature requirement decreases the test times. The nozzle exit to Ludwieg tube diameter ratio is nearly constant for various test Mach numbers while the throat to Ludwieg tube diameter ratio decreases for increasing Mach number.

Modern numerical methods are employed to solve the unsteady quasi-one-dimensional Euler equations. Fifth-order WENO interpolation is carried out on the characteristic variables and an HLLC Riemann solver is utilized to compute the flux. Further schemes are employed to sharpen the resolution of the contact surface. Time integration is carried out with the third-order TVD Runge-Kutta scheme. The

moving boundary of the piston is accounted for by the third-order accurate, inverse Lax-Wendroff procedure of Tan and Shu [44]. The calorically perfect gas assumption is relaxed, and the thermally perfect equations are solved using an application of the energy relaxation method by Montarnal and Shu [33]. The numerical methods employed have been verified to accurately capture the one-dimensional and unsteady, gasdynamic processes.

The numerical results predict the presence of pressure oscillations originating from the highly unsteady piston compression cycle. Ideal equations are used to predict the fill pressures within the secondary reservoir and the compression tube such that the piston achieves full compression while attaining zero velocity at the end of its compression cycle. Although these results overshoot the final piston displacement, they are shown to be an acceptable predictor of fill pressures for the more numerically extensive simulations. These pressures are then utilized to extensively characterize the pressure oscillations for varying piston masses and compression tube lengths. The oscillations are shown to be strongly dependent on the compression completion time. The compression time cycle is increased by using either a heavier piston mass or longer compression tube. The relationship of the piston mass and compression tube with oscillation strength is not entirely monotonic for the presented design space. The numerical results indicate increases in piston mass beyond certain critical masses for a given compression tube length to yield diminishing (and sometimes worsening) returns in dampening the oscillations. This critical mass increases for decreasing compression tube length.

5.2 Contributions

This work has characterized the potential quality of the generating flow for a novel hypersonic facility proposed to be built at the University of Maryland. It has identified configurations which might significantly decrease the steady-flow quality during the expected test-times. A configuration for optimal flow quality has also been suggested for further investigation. The numerical tools applied for this characterization are newly configured for this work, and their application in predicting the unsteady fluid dynamics of this facility has been demonstrated.

5.3 Future Work

Further characterization should be carried out for varying Ludwieg tube lengths, secondary reservoir volumes, secondary reservoir lengths, and Ludwieg tube diameters. A more comprehensive analysis is needed to identify the unsteady waves interactions and isolate the effect of the compression tube to Ludwieg tube area contraction.

Two and three-dimensional unsteady Navier-Stokes simulations are needed to identify flow features not captured by the one-dimensional inviscid Euler equations. Of particular interest are the losses associated with the step-wise area contraction and the stability of the cold-hot gas interface. Experimental validation of the one-dimensional numerical model is currently planned at the Caltech T5 free-piston shock tube facility.

Bibliography

[1] Goyne, C. P., Rodriguez, C. G., Krauss, R. H., McDaniel, J. C., and McClinton, C. R., Experimental and Numerical Study of a Dual-mode Scramjet Combustor, Journal of Propulsion and Power, Vol. 22, No. 3 May 2006, pp. 481-489.

[2] Mitani, T., Hiraiwa, T., Sato, S., Tomioka, S., Kanda, T., and Tani. K., Comparison of Scramjet Engine Performance in Mach 6 Vitiated and Storage-Heated Air, Journal of Propulsion and Power, Vol. 13, No. 5 Sep. 1997, pp. 635-642

[3] Rockwell, R., Goyne, C. P., Haw, W., Krauss, R. H., McDaniel, J. C., and Trefny, C. J., Experimental Study of Test-Medium Vitiation Effects on Dual-Mode Scramjet Performance, Journal of Propulsion and Power, Vol. 27, No. 5 (2011), pp. 1135-1142.

[4] Do, H., Passaro, A., Liu, Q., Lee, T., Baccarella, D., Alta S.p.A., and Gherardesca, V.A., Ethylene Flame Dynamics in an Arc-Heated Hypersonic Wind Tunnel, 51st AIAA Aerospace Sciences Meeting including the New Horizons Forum and Aerospace Exposition 07 - 10 January 2013, Grapevine, Texas

[5] Davis, J.A., Campbell, R.L., and Medley, J.A., Hypervelocity Scramjet Capabilities of the T5 Free-Piston Tunnel at Caltech, AIAA Fourth International Aerospace Planes Conference, 1-4 December, 1992, Orlando, Florida

[6] Heltsley, W.N., Snyder, J.A., Houle, A.J., Davidson, D.F., Mungal, M.G., and Hanson, R.K., Design and Characterization of the Stanford 6 Inch Expansion Tube, 42nd AIAA/ASME/SAE/ASEE Joint Propulsion Conference Exhibit 9 - 12 July 2006, Sacramento, California

[7] Guy, R.W., Rogers, R.C., Rock, K.E., Diskin, G.S., and Puster, R.L., The NASA Langley Scramjet Test Complex, AIAA/ASME/SAE/ASEE Joint Propulsion Conference, 32nd, 1-3 Jul. 1996, Lake Buena Vista, FL, United States

[8] Fotia, M.L., and Driscoll, J.F., Isolator-Combustor Interactions in a Direct-Connect Ramjet-Scramjet Experiment, Journal of Propulsion and Power, Vol. 28, No. 1 (2012), pp. 83-95.

[9] Fischer, K.E., and Rock, K.E., Calculated Effects of Nitric Oxide Flow Contamination on Scramjet Performance, NASA Langley Technical Report Server, 1995, Technical Report

[10] Cummings, R.M., and McLaughlin, T.E., Hypersonic Ludwieg Tube Design and Future Usage at the US Air Force Academy, 50th AIAA Aerospace Sciences Meeting including the New Horizons Forum and Aerospace Exposition 09 - 12 January 2012, Nashville, Tennessee

[11] Oldfield, M.L.G., Jones, T.V., and Schultz, D.L., A Ludwieg Tube with Light Piston Isentropic Compression Heating, Aeronautical Research Council 34 255, 1973.

[12] Kharitonov, A. M., Zvegintsev, V. I., Vasenev, L. G., Kuraeva, A. D., Nalivaichenko, D. G., Novikov, A. V., Paikova, M. A., Chirkashenko, V. F., Shakhmatova, N. V., and Shpak, S. I., Characteristics of the AT-303 hypersonic wind tunnel. Part 1. Velocity Fields, Thermophysics and Aeromechanics Vol. 13, No. 1, 1 Jun. 2001, pp. 1-16.

[13] Eggehs Jr, A.J., One-Dimensional Flows of an Imperfect Diatomic Gas, NACA Report 959, 1950 National Advisory Committee for Aeronautics

[14] Mundt, C., Boyce, R., Jacobs, P., and Hannemann, K., Validation study of numerical simulations by comparison to measurements in piston-driven shock-tunnels, Aerospace and Science Technology, Vol. 11, No. 2-3, Mar. 2007, pp. 100-109.

[15] Houwing, A.F.P., Boyce, R.R., Bone, D.J., and Johnston, D.K. Measurement of recombination rate parameters in nonequilibrium supersonic expansions of ionised argon and neon, Shock Waves, Vol. 1 (1991) pp. 177185.

[16] Paull, A., and Stalker, R.J., Scramjet testing in the T3 and T4 hypersonic impulse facilities, in: E.T. Curran, S.N.B. Murthy (Eds.), Scramjet Propulsion, Progress in Astronautics and Aeronautics, Vol. 189, AIAA, 2000, pp. 146.

[17] Stalker, R.J., and Morgan, R.G., The University of Queensland free piston shock tunnel T4 Initial operation and preliminary calibration, Fourth National Space Engineering Symposium, Adelaide, Australia, 1988.

[18] Hannemann, K., Schneider, M., Reimann, B., and Schramm, J.M., The influence and the delay of driver gas contamination in HEG, AIAA 2000-2595, 21st AIAA Aerodynamic Measurement Technology and Ground Testing Conference, Denver, 1922 June, 2000.

[19] Anderson, J.D., Modern Compressible Flow, 2nd ed., McGraw-Hill Inc., New York, 1990, Chap. 7.

[20] Shapiro, A.H., The Dynamics and Thermodynamics of Compressible Fluid Flow, Vol. 2, The Ronald Press Company, New York, 1954, Chap. 23.

[21] Thompson, P.A., Compressible Fluid Dynamics, McGraw-Hill Inc., New York, 1972, Chap. 23.

[22] Tani, K., Itoh, K., Takahashi, M., Tanno, H., Komuro, T., and Miyajima, H., Numerical Study of Free-Piston Shock Tunnel Performance, Shock Waves, 1994, Vol. 3 pp. 313-319

[23] Parziale, N. J., Rabinovitch, J. , Blanquart, G., Hornung, H. G., and Shepherd, J. E., Propose Vertical Expansion Tunnel, AIAA Journal, Vol. 51, No. 12, Dec. 2013, pp. 2792-2799

[24] Lappas, T., Leonard, A., and Dimotakis, P.E., An Adaptive Lagrangian Method for Computing 1D reacting and Non-Reacting Flows, Journal of Computational Physics, Vol. 104, 1993, pp. 361-376

[25] Jacobs, P.A., Quasi-One-Dimensional Modeling of a Free-Piston Shock Tunnel, AIAA Journal Vol. 32, No. 1, Jan. 1994, pp. 19-23.

[26] Jiang, G.S., and Shu, C.W., Efficient Implementation of Weighted ENO Schemes, Journal of Computational Physics Vol. 126, No. 1, Jun. 1996, pp. 202-228.

[27] Liu, X.D., Osher, S., and Chan, T., Weighted Essentially Non-oscillatory Schemes, Journal of Computational Physics Vol. 115, No. 1, Nov. 1994, pp. 200-228.

[28] Toro, E.F., Spruce, M., and Speares, W., Restoration of the Contact Surface in the HLL-Riemann Solver, Shock Waves Vol. 4, No. 1, Jul. 1994, pp. 25-34.

[29] Toro, E.F., A Linearised Riemann Solver for the TimeDependent Euler Equations of Gas Dynamics, Proc. Roy. Soc. London,1991, pp. 683693.

[30] Roe, P. L., Approximate Riemann Solvers, Parameter Vectors, and Difference Schemes, Journal of Computational Physics, Vol. 43, 1981, pp. 357372.

[31] Harten, A., Engquist, B., Osher, S., Chakravarthy, S.R., Uniformly high order accurate essentially non-oscillatory schemes, Journal of Computational Physics, Vol. 71, No. 2, Aug. 1987, pp. 231-303

[32] Coquel, F., and Benoit, P., Relaxation of Energy and Approximate Riemann Solvers for General Pressure Laws in Fluid Dynamics, SIAM Journal on Numerical Analysis Vol. 35, No. 6, Dec. 1998, pp. 2223-2249.

[33] Montarnal, P., and Shu, C.W., Real Gas Computation Using an Energy Relaxation Method and High-Order WENO Schemes, Journal of Computational Physics Vol. 148, No. 1, 1 Dec. 1999, pp. 59-80.

[34] Liu, Q., and Vasilyev, O.V., A Brinkman penalization method for compressible flows in complex geometries, Journal of Computational Physics, Vol. 227, No. 2, Dec. 10 2007, pp. 946-966.

[35] Shu, C.W., Total-Variation-Diminishing Time Discretizations, SIAM Journal on Scientific and Statistical Computing, Vol. 9, No. 6, Nov. 1988, pp. 1073-1084.

[36] Ingram, D.M., Causon, D.M., and Mingham, C.G., Developments in Cartesian Cut Cell Methods, Mathematics and Computers in Simulation, Vol. 61, 2003, pp. 561-572.

[37] Sotiropoulos, F., and Yang, X., Immersed Boundary Methods for Simulating Fluid-Structure Interaction, Progress in Aerospace Sciences, Vol. 65, 2014, pp. 1-21.

[38] Toro, E., Riemann Solvers and Numerical Methods for Fluid Dynamics, 3rd ed., Springer Dordecht Heidelberg, London, New York

[39] Taylor, E.M., Wu, M., and Martin, M.P., Optimization of Nonlinear Error for Weighted Essentially Non-Oscillatory Methods in Direction Numerical Simulations of Compressible Turbulance, Journal of Computational Physics Vol. 223, No. 2, Apr. 2007, pp. 384-397

[40] Kim, K.H., and Kim, C. Accurate, Efficient, and Monotonic Numerical Methods for Multi-Dimensional Compressible Flows: Part II: Multi-Dimensional Limiting Process, Journal of Computational Physics Vol. 208, No. 2, 20 Sep. 2005, pp. 570-615

[41] Houim, R.W., and Kuo, K.K., A Low-Dissipation and Time-Accurate Method for Compressible Multi-Component Flow with Variable Specific Heat Ratios, Journal of Computational Physics Vol. 230, No. 23, 20 Sep. 2011, pp. 8527-8553

[42] Tan, S., and Shu, C.W., Inverse Lax-Wendroff Procedure for Numerical Boundary Conditions of Conservation Laws, Journal of Computational Physics Vol. 229, No. 21, 20 Oct. 2010, pp. 8144-8166

[43] Tan, S., Wang, C., Shu, C.W., and Ning, J., Efficient Implementation of High Order Inverse Lax-Wendroff Boundary Treatment for Conservation Laws, Journal of Computational Physics Vol. 231, No. 6, 20 Mar. 2012, pp. 2510-2527

[44] Tan, S., and Shu, C.W., A High Order Moving Boundary Treatment for Compressible Inviscid Flows, Journal of Computational Physics Vol. 230, No. 15, 1 Jul. 2011, pp. 6023-6036

[45] Shu, C.W., High Order Weighted Essentially Non-oscillatory Schemes for Convection Dominated Problems, SIAM Review, Vol. 51, No. 1, pp. 82-126.

[46] Borges, R., Carmona, M., Costa, B., and Don, W.S., An Improved Weighted Essentially Non-Oscillatory Scheme for Hyperbolic Conservation Laws, Journal of Computational Physics Vol. 227, No. 6, 1 Mar. 2008, pp. 3191-3211